The Time Evolution of Water Vapor "Black Holes" in the Upper Troposphere

Edwin P. Gerber*

1 Introduction

The water vapor channels on the United States' GOES 10 and GOES 8, the European METEOSAT, and the Japanese GMS geostationary satellites measure long-wave radiation of wavelength 5.7–7.1 μm. Images at these wavelengths do not show any surface features of the Earth, since the radiation emitted by the surface at 5.7–7.1 μm is entirely absorbed by low-level atmospheric water vapor. Rather, they reveal planetary and synoptic scale variations of water vapor in the middle and upper troposphere.

In regions of subsidence, where the large-scale vertical motion is downward, the troposphere becomes filled with dry air from the upper troposphere, and the 5.7–7.1 μm radiation received by the satellite comes primarily from the relatively warm lower troposphere. When the large-scale vertical motion is upward, the cold upper troposphere becomes saturated (or nearly so) with humid air from the surface, and the 5.7–7.1 μm radiation seen by the satellites is the cold water vapor in the upper troposphere. In this way the "equivalent black body temperature" of the 5.7–7.1 μm radiation is a proxy for the vertical motion field. An empirical connection between water vapor and vertical motion is confirmed in [9] and [11], in which a correlation is found between convergence of the mean circulation of the upper troposphere (implying subsidence, by continuity) and dry regions in the satellite images.

In the absence of tropical storms, water vapor images of the low latitude East Pacific are often dominated by two features, the moisture rich Intertropical Convergence Zone (ITCZ) and "black holes," vast regions of low humidity. As shown in Figures 1-3, images taken during the northern hemisphere summer, the ITCZ forms a band of convection across the thermal equator in the East Pacific, centered at approximately 8^0 N. North and south of the ITCZ are the arid regions, centered, in Figure 1, at 145^0 W, 16^0 N and 130^0 W, 8^0 S. The black hole in the southern (winter) hemisphere is comparable in size to the continental United States. In the far west we see a second region of deep convection over Indonesia, associated with the warm La Nina West Pacific.

We seek to explain the shape, particularly the north-south and east-west asymmetries, the intensity, and the time evolution of these East Pacific water vapor black holes as a product of the circulation driven by deep convection in the ITCZ. In the spirit of this

*with Takamitsu Ito and Wayne Schubert

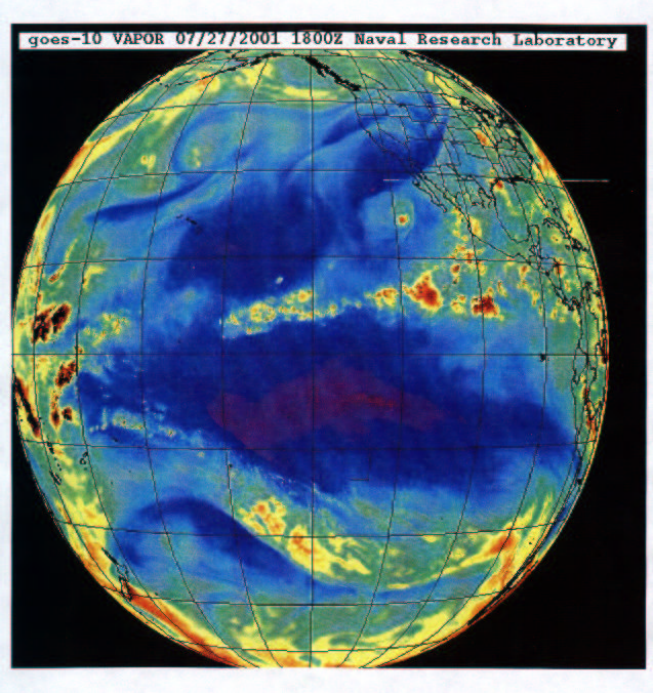

Figure 1: GOES 10 Water Vapor Image, July 27, 2001 1800z. The longitude and latitude interval is 15^0. The center meridian is 135^0 W, and crosses the equator at the center of the image. Green, yellow, and red indicate areas where the upper troposphere is rich in moisture (increasing from green to red). Blue, purple, and black colors indicate an increasingly dry upper troposphere.

summer's GFD program, we have built a conceptual model of the tropical atmosphere to aid us.

1.1 The Basic Model

We begin with stratified β-plane atmosphere extending to infinity in both x and y. We next linearize about a basic state at rest and perform a vertical mode transformation, as in [1]. This separates the motion of the atmosphere into baroclinic modes, each obeying an independent set of equations equivalent to the linearized shallow water system.

We next assume that the latent heat release excites only the first baroclinic mode. The vertical profile of the first mode takes a form similar to a cosine wave from 0 to π. Fluid on the bottom flows opposite that on top, connected by a smooth profile with no motion at a node near the midpoint of the atmosphere. We can view the shallow water equations as prescribing flow at the base of the atmosphere, and then use the sinusoidal vertical profile to complete the picture. Deep convection in this simple system has the effect of transferring mass from the lower layer to the upper layer. We thus prescribe a mass sink in our lower layer to model the effect of the ITCZ, or any other regions of deep convection. Given our forcing, we solve for the resulting subsidence field, and hence the water vapor field, to find the black holes.

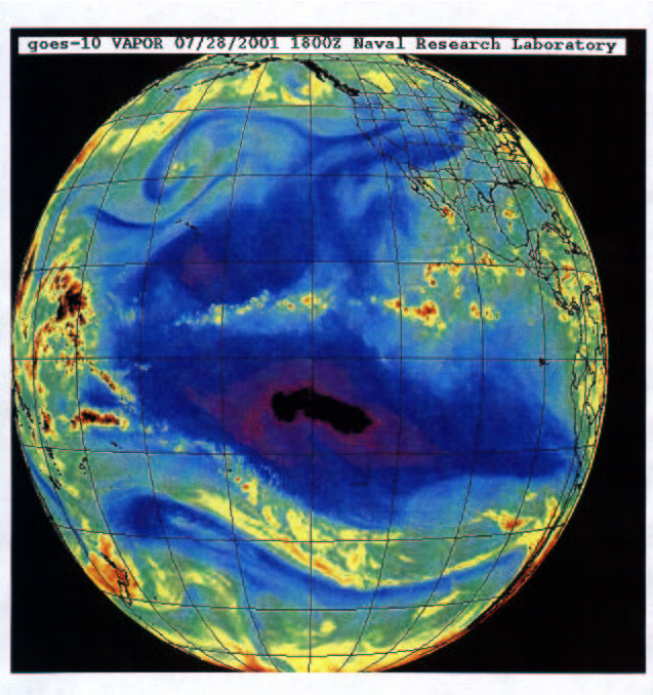

Figure 2: GOES 10 Water Vapor Image, July 28, 2001 1800z

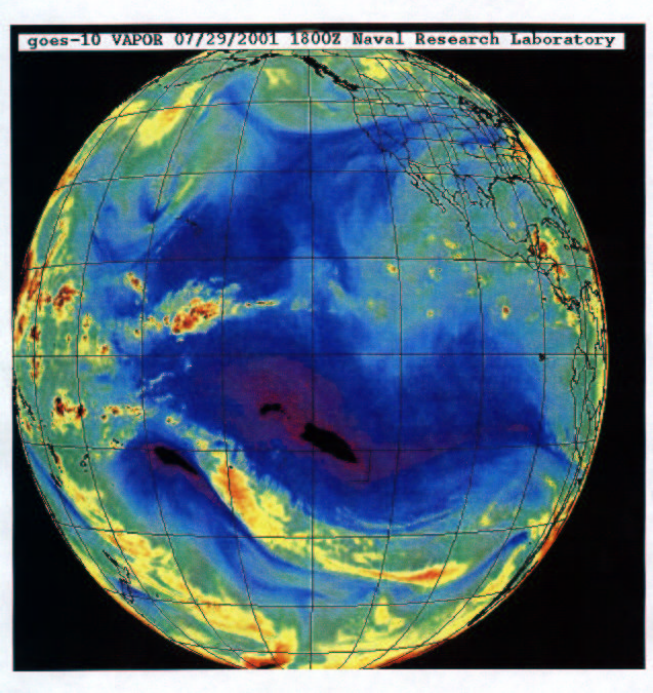

Figure 3: GOES 10 Water Vapor Image, July 29, 2001 1800z

We are following in the footsteps of A. E. Gill, who with others studied this model extensively in the 1980's in [2], [5], and [8]. We do not, however, make the long wave approximation, following rather the original eigenvalue formulation of Matsuno [7] in 1966, later developed in [12], where the time dependent evolution of tropical circulation around the amazon basin was studied. In contrast to [12], however, we attempt to include dissipation and Newtonian cooling in our model. We are thus applying a tried and true theory, seeking to focus a new application; the formation of water vapor black holes.

2 Theory

2.1 The Linearized Equatorial β-Plane

Consider the motions of an incompressible, forced, shallow water fluid on the equatorial β-plane. In our model, this shallow water layer corresponds to the lower layer in the first baroclinic mode. The governing equations, linearized about a resting basic state, are

$$\frac{\partial u}{\partial t} - \beta y v + g\frac{\partial h}{\partial x} = -\epsilon u, \tag{1}$$

$$\frac{\partial v}{\partial t} + \beta y u + g\frac{\partial h}{\partial y} = -\epsilon v, \tag{2}$$

$$\frac{\partial h}{\partial t} + \bar{h}\left(\frac{\partial u}{\partial x} + \frac{\partial v}{\partial y}\right) = -\epsilon h - S, \tag{3}$$

where u and v are velocity components in the x- and y-directions, respectively, h is the deviation of the fluid depth from the constant mean depth $\bar{h}$, βy is the Coriolis parameter, ϵ is the constant Rayleigh friction and Newtonian damping coefficient, and $S(x, y, t)$ is the lower layer mass sink. Before solving (1)–(3) it is convenient to put the problem in nondimensional form. We define $c = (g\bar{h})^{\frac{1}{2}}$ as the constant gravity wave speed based on the mean depth $\bar{h}$. As a horizontal length scale let us choose $L = (c/\beta)^{\frac{1}{2}}$. Similarly, let us choose as a unit of time $T = (\beta c)^{-\frac{1}{2}}$. Data from the ITCZ in the Pacific (specifically the Marshall Islands) and in the Atlantic [1] suggests that, for the first baroclinic mode, $c \approx 7.5 \times 10^1\, m/s$ and $\bar{h} \approx 5.7 \times 10^2\, m$, so that $L \approx 1.8 \times 10^3 km$ and $T \approx 0.28\, day$. For now, we choose c as the unit of speed and $\bar{h}$ as the unit of depth, so that (1)–(3) reduce to the nondimensional form

$$\frac{\partial u}{\partial t} - yv + \frac{\partial h}{\partial x} = -\epsilon u, \tag{4}$$

$$\frac{\partial v}{\partial t} + yu + \frac{\partial h}{\partial y} = -\epsilon v, \tag{5}$$

$$\frac{\partial h}{\partial t} + \frac{\partial u}{\partial x} + \frac{\partial v}{\partial y} = -\epsilon h - S, \tag{6}$$

where all the independent variables x, y, t, all the dependent variables u, v, h, the parameter ϵ and the function $S(x, y, t)$ are now nondimensional. The system (4)–(5) can also be written in the more compact form

$$\frac{\partial \mathbf{w}}{\partial t} + \mathcal{L}\mathbf{w} = -\epsilon \mathbf{w} - \mathbf{S}, \tag{7}$$

where

$$\mathbf{w}(x,y,t) = \begin{pmatrix} u(x,y,t) \\ v(x,y,t) \\ h(x,y,t) \end{pmatrix}, \quad \mathbf{S}(x,y,t) = \begin{pmatrix} 0 \\ 0 \\ S(x,y,t) \end{pmatrix}, \quad \mathcal{L} = \begin{pmatrix} 0 & -y & \partial/\partial x \\ y & 0 & \partial/\partial y \\ \partial/\partial x & \partial/\partial y & 0 \end{pmatrix}. \quad (8)$$

The potential vorticity (PV) principle associated with (4)–(6) is

$$\frac{\partial q}{\partial t} + v = -\epsilon q + yS, \quad (9)$$

where

$$q = \frac{\partial v}{\partial x} - \frac{\partial u}{\partial y} - yh \quad (10)$$

is the potential vorticity anomaly. The total energy principle associated with (4)–(6) is

$$\frac{\partial}{\partial t}\left[\tfrac{1}{2}\left(u^2+v^2+h^2\right)\right] + \frac{\partial (uh)}{\partial x} + \frac{\partial (vh)}{\partial y} = -2\epsilon\left[\tfrac{1}{2}\left(u^2+v^2+h^2\right)\right] - hS, \quad (11)$$

or, in integral form

$$\frac{\partial}{\partial t}\int_{-\infty}^{\infty}\int_{-\infty}^{\infty} \tfrac{1}{2}\left(u^2+v^2+h^2\right) dxdy = -2\epsilon \int_{-\infty}^{\infty}\int_{-\infty}^{\infty} \tfrac{1}{2}\left(u^2+v^2+h^2\right) dxdy - \int_{-\infty}^{\infty}\int_{-\infty}^{\infty} hS dxdy. \quad (12)$$

The energy principle suggests an inner product,

$$(\mathbf{f},\mathbf{g}) = \int_{-\infty}^{\infty} (f_1 g_1^* + f_2 g_2^* + f_3 g_3^*) dy, \quad (13)$$

given

$$\mathbf{f} = \begin{pmatrix} f_1 \\ f_2 \\ f_3 \end{pmatrix}, \qquad \mathbf{g} = \begin{pmatrix} g_1 \\ g_2 \\ g_3 \end{pmatrix}, \quad (14)$$

where we use the * symbol to denote the complex conjugate, anticipating work with complex numbers. We have defined our inner product with respect to y in preparation for a Fourier transform of our equations in x. We may now write our energy principle in more compact form,

$$\int_{-\infty}^{\infty} \frac{1}{2}(\mathbf{w},\mathbf{w}) dx = -2\epsilon \int_{-\infty}^{\infty} \frac{1}{2}(\mathbf{w},\mathbf{w}) dx - \int_{-\infty}^{\infty}\int_{-\infty}^{\infty} hS dxdy. \quad (15)$$

2.2 The Matsuno Eigenvalue Problem

Our goal is to solve (7) for $\mathbf{w}(x,y,t)$ subject to a specified initial condition $\mathbf{w}(x,y,0)$ and mass sink $\mathbf{S}(x,y,t)$. By first solving the inviscid, unforced system,

$$\frac{\partial \mathbf{w}}{\partial t} + \mathcal{L}\mathbf{w} = 0, \quad (16)$$

our goal becomes easier. Let us search for solutions of the form $u(x,y,t) = \mathcal{U}(k,y)e^{i(kx-\omega t)}$, $v(x,y,t) = \mathcal{V}(k,y)e^{i(kx-\omega t)}$, and $h(x,y,t) = \mathcal{H}(k,y)e^{i(kx-\omega t)}$, where k is the zonal wave number and ω the frequency. Hence in our vector notation, we make the substitution

$$\mathbf{w}(x,y,t) = \mathbf{K}(k,y)e^{i(kx-\omega t)}, \tag{17}$$

where

$$\mathbf{K}(k,y) = \begin{pmatrix} \mathcal{U}(k,y) \\ \mathcal{V}(k,y) \\ \mathcal{H}(k,y) \end{pmatrix}, \tag{18}$$

into (16). The substitution results in the eigenvalue problem,

$$-i\omega\mathbf{K} + \hat{\mathcal{L}}\mathbf{K} = 0, \tag{19}$$

where

$$\hat{\mathcal{L}} = \begin{pmatrix} 0 & -y & ik \\ y & 0 & d/dy \\ ik & d/dy & 0 \end{pmatrix}. \tag{20}$$

The adjoint of $\hat{\mathcal{L}}$ with respect to the inner product (13) is the operator $\hat{\mathcal{L}}^\dagger$ which satisfies

$$(\hat{\mathcal{L}}\mathbf{f}, \mathbf{g}) = (\mathbf{f}, \hat{\mathcal{L}}^\dagger\mathbf{g}) \tag{21}$$

for all $\mathbf{f}(y)$ and $\mathbf{g}(y)$ satisfying the boundary conditions, that is $(f,g) < \infty$. Our operator $\hat{\mathcal{L}}$ is skew-Hermitian, as $\hat{\mathcal{L}}^\dagger = -\hat{\mathcal{L}}$, so that (21) becomes

$$(\hat{\mathcal{L}}\mathbf{f}, \mathbf{g}) = -(\mathbf{f}, \hat{\mathcal{L}}\mathbf{g}). \tag{22}$$

The skew-Hermitian property dictates that the eigenvalues of $\hat{\mathcal{L}}$ are purely imaginary, so that we have a mathematical basis for looking for wave-like solutions (solutions where ω is purely real). In addition, the eigenfunctions form a complete orthogonal set. Hence there exist a set of eigenfunctions $\mathbf{K_i}$ that span all functions f satisfying $(f,f) < \infty$ with

$$(\mathbf{K_i}, \mathbf{K_j}) = 0 \tag{23}$$

if $i \neq j$.

The eigenvalue problem was solved in [7], which revealed that (19) has bounded solutions as $y \to \pm\infty$, only if $\omega^2 - k^2 - k/\omega$ is an odd integer, that is, only if

$$\omega^2 - k^2 - k/\omega = 2n + 1, \tag{24}$$

with $n = 0, 1, 2, \ldots$ We shall denote the solutions of this cubic equation by $\omega_{n,r}$, since the frequency will depend on the particular odd integer $2n+1$ chosen, and where the subscript $r = 0, 1, 2$ indicates which of the three roots of the frequency equation we are discussing.

For $n > 0$ our dispersion relation (24) separates nicely into three modes: low frequency Rossby waves which always propagate to the west (ω has the opposite sign of k) and high frequency westward and eastward propagating inertial gravity waves. We have given the

modes the subscripts 0, 1, and 2, respectively. Approximate values for the frequencies are given below. They are more accurate for large n.

$$\omega_{n,0} \approx \frac{-k}{k^2+2n+1} \tag{25}$$

$$\omega_{n,1} \approx -(k^2+2n+1)^{\frac{1}{2}} \tag{26}$$

$$\omega_{n,2} \approx (k^2+2n+1)^{\frac{1}{2}} \tag{27}$$

For $n=0$, (24) factors to $(\omega_{0,r}+k)(\omega_{0,r}^2-k\omega_{0,r}-1)=0$, yielding two mixed modes and one forbidden mode $\omega_{0,1}=-k$ that cannot be normalized. The allowable waves have Rossby and gravity wave character.

$$\omega_{0,0} = \frac{k-(k^2+4)}{2} \tag{28}$$

$$\omega_{0,2} = \frac{k+(k^2+4)}{2} \tag{29}$$

Let $\mathbf{K_{n,r}}$ denote the eigenfunction corresponding to rth root of (24) given n.

$$\mathbf{K_{n,r}} = A_{n,r}e^{-\frac{1}{2}y^2}\begin{pmatrix} -\frac{1}{2}(\omega_{n,r}+k)H_{n+1}(y) - n(\omega_{n,r}-k)H_{n-1}(y) \\ i(\omega_{n,r}^2-k^2)H_n(y) \\ -\frac{1}{2}(\omega_{n,r}+k)H_{n+1}(y) + n(\omega_{n,r}-k)H_{n-1}(y)\end{pmatrix}, \tag{30}$$

where

$$A_{n,r} = \pi^{-\frac{1}{4}}\{2^n n![(n+1)(\omega_{n,r}+k)^2 + n(\omega_{n,r}-k)^2 + (\omega_{n,r}^2-k^2)^2]\}^{-\frac{1}{2}} \tag{31}$$

is a normalization constant which assures that

$$(\mathbf{K_{n,r}}, \mathbf{K_{n,r}}) = 1 \tag{32}$$

The Hermite polynomials $H_n(y)$ are given by $H_0(y)=1$, $H_1(y)=2y$, $H_2(y)=4y^2-2$, $H_3(y)=8y^3-12y$, $\cdots$, with recurrence relation $H_{n+1}(y)=2yH_n(y)-2nH_{n-1}(y)$.

We have not quite found all the solutions of (19), because it is possible to have the trivial solution $\mathcal{V}=0$, but nontrivial $\mathcal{U}$ and $\mathcal{H}$. If we expand (19) with $\mathcal{V}=0$ we find that

$$-\omega\mathcal{U} + k\mathcal{H} = 0 \tag{33}$$

$$y\mathcal{U} + \frac{d\mathcal{H}}{dy} = 0 \tag{34}$$

$$-\omega\mathcal{H} + k\mathcal{U} = 0. \tag{35}$$

The first and third of these can be considered as two linear, homogeneous algebraic equations for $\mathcal{U}$ and $\mathcal{H}$. Requiring the determinant of the coefficients to vanish gives $\omega^2=k^2$, with solutions $\omega=\pm k$. When $\omega=-k$, $\mathcal{H}=-\mathcal{U}$ and (34) becomes $d\mathcal{U}/dy=y\mathcal{U}$, with solution $\mathcal{U}\sim e^{\frac{1}{2}y^2}$. This solution must be discarded since it is not bounded as $y\to\pm\infty$. When $\omega=k$, $\mathcal{H}=\mathcal{U}$ and (34) becomes $d\mathcal{U}/dy=-y\mathcal{U}$, with solution $\mathcal{U}\sim e^{-\frac{1}{2}y^2}$. This solution is acceptable. Thus, we have found the additional (Kelvin wave) eigenfunction

$$\mathbf{K_{-1}} = A_{-1}e^{-\frac{1}{2}y^2}\begin{pmatrix}1\\0\\1\end{pmatrix}, \tag{36}$$

with corresponding eigenvalue (dispersion relation) $\omega_{-1}=k$. The subscript -1 is chosen because the dispersion relation $\omega=k$ is a solution of $\omega^2-k^2-k/\omega=2n+1$ when $n=-1$.

2.3 The Normal Mode Transformation

We may now use our eigenfunctions to decompose the forced, damped problem into normal modes. First, we introduce the Fourier transform pair in x,

$$u(x,y,t) = (2\pi)^{-\frac{1}{2}} \int_{-\infty}^{\infty} \hat{u}(k,y,t) e^{ikx} dk, \tag{37}$$

$$\hat{u}(k,y,t) = (2\pi)^{-\frac{1}{2}} \int_{-\infty}^{\infty} u(x,y,t) e^{-ikx} dx, \tag{38}$$

where k is the zonal wavenumber. Similar transform pairs exist for $v(x,y,t)$ and $\hat{v}(k,y,t)$, for $h(x,y,t)$ and $\hat{h}(k,y,t)$, and for $S(x,y,t)$ and $\hat{S}(k,y,t)$. We can now write (7) as

$$\frac{\partial \hat{\mathbf{w}}}{\partial t} + \hat{\mathcal{L}}\hat{\mathbf{w}} = -\epsilon \hat{\mathbf{w}} - \hat{\mathbf{S}}, \tag{39}$$

where

$$\hat{\mathbf{w}}(k,y,t) = \begin{pmatrix} \hat{u}(k,y,t) \\ \hat{v}(k,y,t) \\ \hat{h}(k,y,t) \end{pmatrix}, \qquad \hat{\mathbf{S}}(k,y,t) = \begin{pmatrix} 0 \\ 0 \\ \hat{S}(k,y,t) \end{pmatrix}, \tag{40}$$

and $\hat{\mathcal{L}}$ is defined as in (20).

Our second task is to transform (39) in y. As our eigenfunctions $\mathbf{K}_{n,r}(k,y)$ satisfy the orthonormality condition

$$\left(\mathbf{K}_{n,r}(k,y), \mathbf{K}_{n',r'}(k,y)\right) = \begin{cases} 1 & (n',r') = (n,r) \\ 0 & (n',r') \neq (n,r) \end{cases}, \tag{41}$$

we can set up a transform pair

$$\hat{w}_{n,r}(k,t) = \left(\hat{\mathbf{w}}(k,y,t), \mathbf{K}_{n,r}(k,y)\right), \tag{42}$$

$$\hat{\mathbf{w}}(k,y,t) = \sum_{n,r} \hat{w}_{n,r}(k,t) \mathbf{K}_{n,r}(k,y). \tag{43}$$

Taking the inner product of (39) with $\mathbf{K}_{n,r}(k,y)$, we obtain

$$\begin{aligned}
\left(\frac{\partial \hat{\mathbf{w}}(k,y,t)}{\partial t}, \mathbf{K}_{n,r}(k,y)\right) + \left(\hat{\mathcal{L}}\hat{\mathbf{w}}(k,y,t), \mathbf{K}_{n,r}(k,y)\right) &= \\
-\epsilon \left(\hat{\mathbf{w}}(k,y,t), \mathbf{K}_{n,r}(k,y)\right) - \left(\hat{\mathbf{S}}(k,y,t), \mathbf{K}_{n,r}(k,y)\right) & \\
\frac{\partial}{\partial t}\left(\hat{\mathbf{w}}(k,y,t), \mathbf{K}_{n,r}(k,y)\right) - \left(\hat{\mathbf{w}}(k,y,t), \hat{\mathcal{L}}\mathbf{K}_{n,r}(k,y)\right) &= -\epsilon \hat{w}_{n,r}(k,t) - \hat{S}_{n,r}(k,t) \\
\frac{d\hat{w}_{n,r}(k,t)}{dt} - \left(\hat{\mathbf{w}}(k,y,t), i\omega_{n,r}\mathbf{K}_{n,r}(k,y)\right) &= -\epsilon \hat{w}_{n,r}(k,t) - \hat{S}_{n,r}(k,t) \\
\frac{d\hat{w}_{n,r}(k,t)}{dt} + i\omega_{n,r}\left(\hat{\mathbf{w}}(k,y,t), \mathbf{K}_{n,r}(k,y)\right) &= -\epsilon \hat{w}_{n,r}(k,t) - \hat{S}_{n,r}(k,t)
\end{aligned}$$

so that

$$\frac{d\hat{w}_{n,r}(k,t)}{dt} + (\epsilon + i\omega_{n,r})\hat{w}_{n,r}(k,t) = -\hat{S}_{n,r}(k,t). \tag{44}$$

Equation (44) is the transformation to spectral space of the original system (7) and has solution

$$\hat{w}_{n,r}(k,t) = \hat{w}_{n,r}(k,0)e^{-(\epsilon+i\omega_{n,r})t} - \int_0^t \hat{S}_{n,r}(k,t')e^{-(\epsilon+i\omega_{n,r})(t-t')}dt'. \tag{45}$$

When this spectral space solution is inserted into (43), we obtain the vector equation

$$\hat{\mathbf{w}}(k,y,t) = \sum_{n,r} \hat{w}_{n,r}(k)\mathbf{K}_{n,r}(k,y), \tag{46}$$

Taking the inverse Fourier transform of (46) and breaking back into component form, we obtain our final physical space solutions

$$u(x,y,t) = (2\pi)^{-\frac{1}{2}} \int_{-\infty}^{\infty} \sum_{n,r} \hat{w}_{n,r}(k)\mathcal{U}_{n,r}(k,y)e^{ikx}dk, \tag{47}$$

$$v(x,y,t) = (2\pi)^{-\frac{1}{2}} \int_{-\infty}^{\infty} \sum_{n,r} \hat{w}_{n,r}(k)\mathcal{V}_{n,r}(k,y)e^{ikx}dk, \tag{48}$$

$$h(x,y,t) = (2\pi)^{-\frac{1}{2}} \int_{-\infty}^{\infty} \sum_{n,r} \hat{w}_{n,r}(k)\mathcal{H}_{n,r}(k,y)e^{ikx}dk. \tag{49}$$

According to (47) – (49) the general solution of our initial value problem consists of a superposition of normal modes. The superposition involves all zonal wavenumbers (integral over k), all meridional wavenumbers (sum over n), and all wave types (sum over r).

It should be noted that typical superpositions of many normal modes result in spatial patterns which differ greatly from individual normal modes. We found that the $w_{n,r}$ decay exponentially with n for all choices of k. Thus, given a specified degree of accuracy, we can select an N so that the partial sum of all modes $n < N$ meets the requirement. In general, we found that $N = 200$ gave very good results.

It was also necessary to perform the Inverse Fourier Transform via a numeric approximation to the integral. A simple mid-point rule numeric integration was sufficient.

2.4 Forcing

We consider cases where the time evolution of the forcing is separable from its spatial dependence.

$$S(x,y,t) = (\pi ab)^{-1}e^{-x^2/a^2}e^{-(y-y_0)^2/b^2}\tilde{S}(t), \tag{50}$$

where y_0 is the center of the Gaussian shaped mass sink and a and b control the spatial extent in x and y. The factor $(\pi ab)^{-1}$ has been included so that

$$\int_{-\infty}^{\infty}\int_{-\infty}^{\infty} S(x,y,t)dxdy = \tilde{S}(t), \tag{51}$$

i.e., the rate of total mass removal is independent of the choices of a and b.

The Fourier transform of this forcing is

$$\hat{S}(k,y,t) = (\pi ab)^{-1}(2\pi)^{-\frac{1}{2}} e^{-(y-y_0)^2/b^2} \tilde{S}(t) \int_{-\infty}^{\infty} e^{-x^2/a^2} e^{-ikx} dx \tag{52}$$

$$= 2^{-\frac{1}{2}} (\pi b)^{-1} e^{-(y-y_0)^2/b^2} e^{-\frac{1}{4}k^2a^2} \tilde{S}(t). \tag{53}$$

Then, using (42), we obtain

$$\begin{aligned}
\hat{S}_{n,r}(k,t) &= \left(\hat{\mathbf{S}}(k,y), \mathbf{K}_{n,r}(k,y)\right) = \int_{-\infty}^{\infty} \hat{S}(k,y,t)\mathcal{H}_{n,r}(k,y)dy \\
&= 2^{-\frac{1}{2}}(\pi b)^{-1} e^{-\frac{1}{4}k^2a^2} \tilde{S}(t) \int_{-\infty}^{\infty} e^{-(y-y_0)^2/b^2} \mathcal{H}_{n,r}(k,y)dy \\
&= 2^{-\frac{1}{2}}(\pi b)^{-1} e^{-\frac{1}{4}k^2a^2} A_{n,r} \tilde{S}(t) \\
&\quad \cdot \int_{-\infty}^{\infty} e^{-(y-y_0)^2/b^2} e^{-\frac{1}{2}y^2} \left[-\tfrac{1}{2}(\omega_{n,r}+k)H_{n+1}(y) + n(\omega_{n,r}-k)H_{n-1}(y)\right] dy.
\end{aligned}$$

From [3] we have

$$\int_{-\infty}^{\infty} e^{-(y-y_0)^2/b^2} e^{-\frac{1}{2}y^2} H_n(y)dy = \left(\frac{2\pi b^2}{2+b^2}\right)^{\frac{1}{2}} \left(\frac{2-b^2}{2+b^2}\right)^{\frac{n}{2}} e^{-y_0^2/(2+b^2)} H_n\left(\frac{2y_0}{(4-b^4)^{\frac{1}{2}}}\right) \tag{54}$$

for $0 < b < 2^{\frac{1}{2}}$. (For $b > 2^{\frac{1}{2}}$, there exists a recursion formula to solve the integral, but the modulus of the forcing term will increase with n, making for poor convergence.) Utilizing (54), we finally obtain

$$\begin{aligned}
&\hat{S}_{n,r}(k,t) = \pi^{-\frac{1}{2}} A_{n,r} (2+b^2)^{-\frac{1}{2}} e^{-\frac{1}{4}k^2a^2} e^{-y_0^2/(2+b^2)} \tilde{S}(t) \qquad (55)\\
&\cdot \left\{ -\tfrac{1}{2}(\omega_{n,r}+k) \left(\tfrac{2-b^2}{2+b^2}\right)^{\frac{n+1}{2}} H_{n+1}\left(\tfrac{2y_0}{(4-b^4)^{\frac{1}{2}}}\right) + n(\omega_{n,r}-k)\left(\tfrac{2-b^2}{2+b^2}\right)^{\frac{n-1}{2}} H_{n-1}\left(\tfrac{2y_0}{(4-b^4)^{\frac{1}{2}}}\right) \right\},
\end{aligned}$$

for all modes with the exception of the Kelvin wave, which takes a similar (and simpler) form.

To focus on the time dependence, (55) can be viewed as a function $\breve{S}_{n,r}$ of n, r, k, a, and b multiplying the time dependent part,

$$\hat{S}_{n,r}(k,t) = \breve{S}_{n,r}(k)\tilde{S}(t). \tag{56}$$

If we separate $\hat{w}_{n,r}(k,t) = \breve{w}_{n,r}(k)\tilde{w}_{n,r}(t)$ also, (44) yields,

$$\breve{w}_{n,r}(k)\left(\frac{d\tilde{w}_{n,r}(t)}{dt} + (\epsilon + i\omega_{n,r})\tilde{w}_{n,r}(t)\right) = -\breve{S}_{n,r}(k)\tilde{S}(t) \tag{57}$$

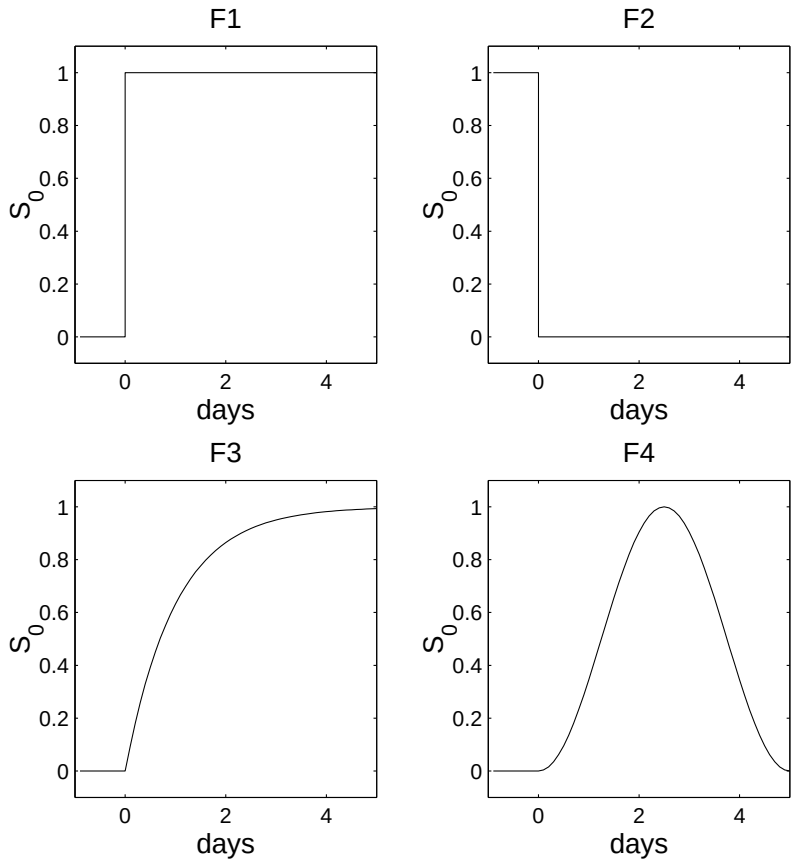

Figure 4: $\tilde{S}(t)$

We can now take $\breve{w}_{n,r}(k) = -\breve{S}_{n,r}(k)$, leaving

$$\frac{d\tilde{w}_{n,r}(t)}{dt} + (\epsilon + i\omega_{n,r})\tilde{w}_{n,r}(t) = \tilde{S}(t), \tag{58}$$

which has solution, following (45),

$$\tilde{w}_{n,r}(t) = e^{-(\epsilon+i\omega)t}\left(\int_0^t e^{(\epsilon+i\omega)t'}\tilde{S}(t')dt' + \tilde{w}_{n,r}(0)\right). \tag{59}$$

If $\tilde{S}(t)$ converges to a steady value, $\tilde{S}$, the solution will converge to the steady state solution, where

$$\tilde{w}_{n,r}(t) = \frac{\tilde{S}}{(\epsilon + i\omega)}. \tag{60}$$

We experimented with four different forcing functions, shown in Table 1 (and in Figure 4), hoping to model the onset and termination of convection. Forcing F1 is the Rossby adjustment problem, in which an atmosphere at rest adjust to a sudden, steady release of

Type	$\tilde{S}(t)$	$\tilde{w}_{n,r}(0)$	$\tilde{w}_{n,r}(t)$
F1	S_0	0	$S_0(1-e^{-(\epsilon+i\omega)t})\frac{1}{\epsilon+i\omega}$
F2	0	$\frac{S_0}{(\epsilon+i\omega)}$	$S_0 e^{-(\epsilon+i\omega)t}\frac{1}{\epsilon+i\omega}$
F3	$S_0(1-e^{-\gamma t})$	0	see (61)
F4	$\frac{S_0}{2}(1-cos(\gamma t))$	0	see (63)

Table 1: Forcing Functions

latent heat. Such forcing has been modeled before, but with the long wave approximation [5]. F2 is the adjustment problem in reverse, in which we shut off the heating in an atmosphere in equilibrium with a steady forcing. F3 was chosen as a simple, more realistic way to model the onset of convection. F4 attempts to capture the response to both the onset and termination of heating.

Forcing F3 yielded the following solution,

$$\tilde{w}_{n,r}(t) = S_0\left(\frac{1}{(\epsilon+i\omega_{n,r})} - \frac{e^{-\gamma t}}{(\epsilon-\gamma+i\omega_{n,r})} + \frac{\gamma e^{-(\epsilon+i\omega_{n,r})t}}{(\epsilon^2-\epsilon-\omega_{n,r}^2)+i\omega_{n,r}(2\epsilon-\gamma)}\right). \tag{61}$$

In the the limit $\gamma \gg \epsilon$, that is, when the rate at which the forcing turns on is fast relative to the rate of dissipation, (61) approaches the solution to forcing F1. In the other extreme, $\epsilon \gg \gamma$, (61) reduces to

$$\tilde{w}_{n,r}(t) = \frac{S_0}{(\epsilon+i\omega_{n,r})} - (1-e^{-\gamma t}). \tag{62}$$

in which the atmospheric response is always in equilibrium with the forcing. Forcing F4 results in

$$\tilde{w}_{n,r}(t) = \frac{S_0}{2}\left(\frac{1-e^{-(\epsilon+i\omega_{n,r})t}}{(\epsilon+i\omega_{n,r})} + \frac{(\epsilon+i\omega_{n,r})\left(e^{-(\epsilon+i\omega_{n,r})t}-cos(\gamma t)\right)-\gamma sin(\gamma t)}{(\epsilon+i\omega_{n,r})^2+\gamma^2}\right). \tag{63}$$

In the limit $\epsilon \gg \gamma$ (slow forcing) it reduces to a form similar to (62) in which the response is in equilibrium with the forcing at all times. In the opposite extreme, $\gamma \gg \epsilon$, we find

$$\tilde{w}_{n,r}(t) = S_0\left(\frac{1-e^{-(\epsilon+i\omega_{n,r})t}}{2(\epsilon+i\omega_{n,r})} - \frac{sin(\gamma t)}{2\gamma}\right). \tag{64}$$

The first term on the left hand side corresponds to a system adjusting as in forcing function F1 to the average value of the forcing, $S_0/2$, while the second term corresponds to a small out of phase response to the forcing.

2.5 Subsidence

w_{nd}, the nondimensional upward velocity, can be calculated directly from our shallow water solutions. Shallow water continuity implies that

$$w_{nd} = \frac{\partial h}{\partial t} = -\left(\frac{\partial u}{\partial x} + \frac{\partial v}{\partial y}\right). \tag{65}$$

For the first baroclinic mode, w is zero at the top and bottom of the atmosphere, reaching a maximum near the center. The complete vertical velocity profile takes on a form similar to a sine wave from 0 to π. w_{nd}, once properly dimensionalized, tells us the amplitude of the z-velocity in the first baroclinic mode, and hence corresponds to the maximum velocity found at the center of the vertical profile.

In spectral space,

$$\begin{aligned} \mathcal{W} &= \frac{\partial \mathcal{H}}{\partial t} \\ &= -i\omega\mathcal{H} \end{aligned} \tag{66}$$

for each mode. This enables us to calculate w analytically, the only error coming from the fact that we truncate our sum at the Nth mode.

2.6 Comparison with Gill

The long wave approximation is made in the linearized equatorial β-plane model first proposed by Gill in 1980 [2], and later developed further in [5, 8]. The only difference from our model is that the $\frac{\partial v}{\partial t}$ and $-\epsilon v$ terms are dropped from (2), based on scaling analysis, leaving the modified y-momentum equation

$$\beta y u + g\frac{\partial h}{\partial y} = 0. \tag{67}$$

The y-momentum equation hence reduces to simple geostrophic balance, and adjustment in v becomes instantaneous. (1) and (3) remain the same. While Gill concisely solves this system with the use of parabolic cylinder functions, analysis with Matsuno's eigenfunctions provides insight into the coupling between the inertial gravity and Rossby waves resulting from the long wave approximation. (Note that, as $v = 0$ in the Kelvin wave, it is unaffected by the long wave approximation.)

We proceed with the same analysis as before, applying a Fourier transform in x to reach the Gill equivalent of (39)

$$\frac{\partial}{\partial t}\begin{pmatrix} \hat{u}(k,y,t) \\ 0 \\ \hat{h}(k,y,t) \end{pmatrix} + \hat{\mathcal{L}}\hat{\mathbf{w}} = -\epsilon \begin{pmatrix} \hat{u}(k,y,t) \\ 0 \\ \hat{h}(k,y,t) \end{pmatrix} - \hat{\mathbf{S}}, \tag{68}$$

where $\mathbf{w}$, $\hat{\mathcal{L}}$ and $\mathbf{S}$ are defined as before in (20) and (40). We introduce the matrix

$$\mathbf{F} = \begin{pmatrix} 0 & 0 & 0 \\ 0 & 1 & 0 \\ 0 & 0 & 0 \end{pmatrix} \tag{69}$$

so that we may write (68) in a form more similar to (39), having now just two corrections to account for the long wave approximation

$$\frac{\partial \hat{\mathbf{w}}}{\partial t} - \frac{\partial \mathbf{F}\hat{\mathbf{w}}}{\partial t} + \hat{\mathcal{L}}\hat{\mathbf{w}} = -\epsilon\hat{\mathbf{w}} + \epsilon\mathbf{F}\hat{\mathbf{w}} - \hat{\mathbf{S}}. \tag{70}$$

We now express $\mathbf{w}$ a sum of the $\mathbf{K}_{n,r}$ as in (43) and take the inner product of (70) with a particular $\mathbf{K}_{n',r'}$,

$$\left(\frac{\partial}{\partial t}\sum_{n,r}\hat{w}_{n,r}\mathbf{K}_{n,r},\mathbf{K}_{n',r'}\right)-\left(\frac{\partial}{\partial t}\mathbf{F}\sum_{n,r}\hat{w}_{n,r}\mathbf{K}_{n,r},\mathbf{K}_{n',r'}\right)+\left(\hat{\mathcal{L}}\sum_{n,r}\hat{w}_{n,r}\mathbf{K}_{n,r},\mathbf{K}_{n',r'}\right)=$$

$$-\epsilon\left(\sum_{n,r}\hat{w}_{n,r}\mathbf{K}_{n,r},\mathbf{K}_{n',r'}\right)+\epsilon\left(\mathbf{F}\sum_{n,r}\hat{w}_{n,r}\mathbf{K}_{n,r},\mathbf{K}_{n',r'}\right)-\left(\hat{\mathbf{S}},\mathbf{K}_{n',r'}\right). \tag{71}$$

Applying the orthonormality condition of the $\mathbf{K}_{n,r}$ cleans up most of the terms, yielding a result comparable to (44), modulo our correction.

$$\frac{d\hat{w}_{n',r'}}{dt}+(\epsilon+i\omega_{n',r'})\hat{w}_{n',r'}=-\hat{S}_{n',r'}+\sum_{n,r}\left(\frac{d\hat{w_{n,r}}}{dt}+\epsilon w_{n,r}\right)\left(\mathbf{F}\mathbf{K}_{n,r},\mathbf{K}_{n',r'}\right). \tag{72}$$

Looking closer at our correction term, we have

$$\begin{aligned}\left(\mathbf{F}\mathbf{K}_{n,r},\mathbf{K}_{n',r'}\right) &= \int_{-\infty}^{\infty}\mathcal{V}_{n,r},\mathcal{V}_{n',r'}dy \\ &= A_{n,r}A_{n',r'}(\omega_{n,r}^2-k^2)(\omega_{n',r'}^2-k^2)\int_{-\infty}^{\infty}H_nH_{n'}e^{-y^2}dy. \end{aligned}\tag{73}$$

All is not lost, as the Hermite Polynomials have the property that

$$\int_{-\infty}^{\infty}H_nH_{n'}e^{-y^2}dy=\begin{cases}\pi^{\frac{1}{2}}n!2^n & n=n'\\ 0 & n\neq n'\end{cases}, \tag{74}$$

so that, and making use of the definition of $A_{n,r}$, (31),

$$\left(\mathbf{F}\mathbf{K}_{n,r},\mathbf{K}_{n',r'}\right)=\begin{cases}a_{n',r,r'} & n=n'\\ 0 & n\neq n'\end{cases} \tag{75}$$

with

$$a_{n,r,r'}=\prod_{q=r,r'}\frac{(\omega_{n,q}^2-k^2)}{\left((n+1)(\omega_{n,q}+k)^2+n(\omega_{n,q}-k)^2+(\omega_{n,q}^2-k^2)^2\right)^{\frac{1}{2}}}. \tag{76}$$

In light of these results the summation of n and r in (72) reduces to a sum over just r, yielding

$$\frac{d\hat{w}_{n',r'}}{dt}+(\epsilon+i\omega_{n',r'})\hat{w}_{n',r'}=-\hat{S}_{n',r'}+\sum_{r}a_{n',r,r'}\left(\frac{d\hat{w_{n,r}}}{dt}+\epsilon w_{n,r}\right). \tag{77}$$

The long wave approximation ties the evolution of the gravity and Rossby waves together by coupling $\hat{w}_{n,0}$, $\hat{w}_{n,1}$, and $\hat{w}_{n,0}$. For each n, (77) gives us three coupled ODE's, which can be combined into one matrix differential equation,

$$\mathbf{A}\frac{d\hat{\mathbf{w}}_\mathbf{n}}{dt}+\mathbf{B}\hat{\mathbf{w}}_\mathbf{n}=\hat{\mathbf{S}}_\mathbf{n} \tag{78}$$

where

$$\begin{aligned}
\mathbf{A} &= \begin{pmatrix} 1-a_{n,0,0} & -a_{n,0,1} & -a_{n,0,2} \\ -a_{n,0,1} & 1-a_{n,1,1} & -a_{n,1,2} \\ -a_{n,0,2} & -a_{n,1,2} & 1-a_{n,1,1} \end{pmatrix}, \\
\mathbf{B} &= \begin{pmatrix} \epsilon + i\omega_{n,0} - \epsilon a_{n,0,0} & -\epsilon a_{n,0,1} & -\epsilon a_{n,0,2} \\ -\epsilon a_{n,0,1} & \epsilon + i\omega_{n,1} - \epsilon a_{n,1,1} & -\epsilon a_{n,1,2} \\ -\epsilon a_{n,0,2} & -\epsilon a_{n,1,2} & \epsilon + i\omega_{n,2} - \epsilon a_{n,2,2} \end{pmatrix},
\end{aligned}$$

and

$$\hat{\mathbf{w}}_\mathbf{n} = \begin{pmatrix} \hat{w}_{n,0} \\ \hat{w}_{n,1} \\ \hat{w}_{n,2} \end{pmatrix}, \qquad \hat{\mathbf{S}}_\mathbf{n} = \begin{pmatrix} \hat{S}_{n,0} \\ \hat{S}_{n,1} \\ \hat{S}_{n,2} \end{pmatrix}. \tag{79}$$

We must make an exception when $n = 0$, for there is no $\mathbf{K_{0,1}}$ eigenfunction. In this case we have just two coupled ODE's, which can be represented by an otherwise similar two-dimensional matrix equation.

The steady state solution to (78) is simply

$$\hat{\mathbf{w}}_\mathbf{n} = \mathbf{B^{-1}}\hat{\mathbf{S}}_\mathbf{n}, \tag{80}$$

provided of course that $\mathbf{B}$ is invertible. This is a fair assumption, as the the $a_{n,r,r'}$ corrections are relatively small, so that $\mathbf{B}$ (and $\mathbf{A}$, for that matter) are diagonally dominant. This assumption is not necessarily accurate for the mixed modes corresponding to $n = 0$, and I am not sure we can solve this equation for all forcing functions.

We must make a few more assumptions on the properties of $\mathbf{A}$ and $\mathbf{B}$ to solve the time dependent version of (78). We first multiply by $\mathbf{A^{-1}}$ to obtain

$$\frac{d\hat{\mathbf{w}}_\mathbf{n}}{dt} + \mathbf{A^{-1}B}\hat{\mathbf{w}}_\mathbf{n} = \mathbf{A^{-1}}\hat{\mathbf{S}}_\mathbf{n}. \tag{81}$$

Next assume that $\mathbf{A^{-1}B}$ is diagonizable, so that there exist a constant, invertible matrix $\mathbf{P}$ such that,

$$\mathbf{PA^{-1}BP^{-1}} = \mathbf{D}, \tag{82}$$

with $\mathbf{D}$ diagonal. We then multiply (81) by $\mathbf{P}$, in preparation for defining a new time dependent vector $\mathbf{q_n}(t) = \mathbf{P}\hat{\mathbf{w}}_\mathbf{n}(t)$ so that

$$\begin{aligned}
\frac{d\mathbf{P}\hat{\mathbf{w}}_\mathbf{n}}{dt} + \mathbf{PA^{-1}BP^{-1}P}\hat{\mathbf{w}}_\mathbf{n} &= \mathbf{PA^{-1}}\hat{\mathbf{S}}_\mathbf{n} &(83)\\
\frac{d\mathbf{q_n}}{dt} + \mathbf{D}\mathbf{q_n} &= \mathbf{PA^{-1}}\hat{\mathbf{S}}_\mathbf{n}. &(84)
\end{aligned}$$

In (84) we have decoupled the ODE's, so that each component of $\mathbf{q_n}$ may be solved individually with the same techniques used to solve (44), or, more elegantly, solved with a matrix exponential,

$$\mathbf{q_n} = \mathbf{e^{-Dt}}\mathbf{q_n}(0) + \mathbf{e^{-Dt}}\int_0^t \mathbf{e^{Dt'}PA^{-1}}\hat{\mathbf{S}}_\mathbf{n}dt'. \tag{85}$$

Note that as $\mathbf{D}$ is diagonal,

$$\mathbf{e^{Dt}} = \begin{pmatrix} e^{d_1 t} & 0 & 0 \\ 0 & e^{d_2 t} & 0 \\ 0 & 0 & e^{d_3 t} \end{pmatrix}. \tag{86}$$

Lastly, we obtain our coefficients

$$\hat{\mathbf{w}}_\mathbf{n}(t) = \mathbf{P^{-1}} \mathbf{q_n}(t). \tag{87}$$

3 Results

3.1 The East Pacific, July 27-29, 2001

Figures 1, 2, and 3 reveal two large water vapor black holes evolving over the East Pacific. In the first image, taken on July 27 at 1800z, we see the East Pacific ITCZ spanning over 6000 km, from 150^0 W to Central America. The convection begins at 5^0 N in the west and rises to 15^0 N in the east, its meridional extent varying from 500 to 1000 km. This position of the ITCZ is typical during the northern hemisphere summer, as the ITCZ tends to follow the thermal equator. Another large region of deep convection is visible at the western edge of the image, centered over Papua New Guinea and Indonesia. Convection in this area is especially strong during La Nina years. To the east we see a bit of seasonal convection over the Amazon basin, and in the south, the South Pacific Convergence Zone (SPCZ) stretches northwest to southeast from 165^0 W, 15^0 S to 120^0 W, 40^0 S.

A large, arid black hole centered at 130^0 W, 7^0 S has already formed to south of the East Pacific ITCZ, spanning nearly 80 degrees of longitude. At is widest point it spans nearly 30^0 of latitude, over 3000 km. A smaller dry region has formed northwest of the the East Pacific ITCZ, centered near 145^0 W, 16^0 N.

The large black hole in the south reaches its apex 24 hours later on the 28th, Figure 2. The East Pacific ITCZ has extended further to the west, now stretching past 155^0 W. The broader convection in the east is still present. The southern black hole has intensified, especially in the center, where we now see a "black hole" in the image. The northern black hole has also increased in size, its eastern boundary now 500 km further west at 165^0 W.

The broad convection in the eastern half of the ITCZ, especially between 120 and 105^0 W, weakens by the 29th, as shown in Figure 3. Unfortunately for our linear theory, advection seems to be playing a large role now. Intense convection in the ITCZ is now only in the west, where it begins to merge into the West Pacific convection. The southern black hole has been contorted, and has shrunk slightly. The northern black hole is less affected, though it has been pushed slightly north by a new burst of convection.

3.2 Setting up the Model

We must model this complicated system with Gaussian regions of convection, as given by (50). To simulate the East Pacific ITCZ, we selected parameters a and b to create an elongated convection region with Gaussian folding distances in x and y of 2700 and 450 km, respectively. y_0 was selected so that the convection would be centered at 10.5^0 N.

The parameter ϵ determines both the momentum damping and Newtonian cooling rates in our model. Following Gill, we based our value on the momentum damping rate, taking $\epsilon = \frac{1}{3days}$ [2]. ($\epsilon = \frac{1}{10days}$ would be more appropriate for the Newtonian cooling rate. See the Fellow's report by Takamitsu Ito for a simulation in which this problem has been remedied.) S_0, the dimensional heating rate for the first baroclinic mode, is 57 m/day [1]. This value is based on measurements taken over the Marshall Islands in the Pacific and from the GATE survey of the Atlantic.

Note that we used a partial summation of normal modes truncated at $N = 200$ in all the data we present. We approximated the Inverse Fourier Transform, an integral over wavenumber k from $-\infty$ to ∞, as a numeric integral from -10 to 10 with 128 point resolution. The truncation of the integral is based on the fact that the Fourier transform decays as $e^{\frac{-a^2k^2}{4}}$. We projected our β-plane solutions, which span to infinity in all directions, onto maps by ignoring the sphericity of the globe in the tropics. The maps are included to provide a better sense of scale and positioning.

The steady state subsidence field for the East Pacific ITCZ (labeled region A) is shown in the top half of Figure 5. We show only contours of downward velocity, in units m/day. This is the velocity at the center of the atmospheric column, where it is largest for the first baroclinic mode. While the greatest subsidence rate is not even 2 m/day, the maximum upward motion exceeds 50 m/day. If we equate drier air with greater subsidence, we already see the basic features of Figures 1 - 3; two large subsidence regions with significant zonal and meridional asymmetries with respect to the ITCZ.

To better compare our simulation with observations, we also included a first approximation to the convection over the West Pacific. Convection in the region appears much more stable, in bulk, through our observational period. We thus included a steady state convection cell over Papua New Guinea as a backdrop for our time dependent simulation. (A linear theory allows one to paste solutions together!) We centered this convection region on the equator at 160^0 E, with Gaussian folding distance of 900 km in both x and y. The complete steady state subsidence field is shown in the lower half of Figure 5. Again, we show only contours of downward velocity. A comparison with the upper half of the figure reveals that the West Pacific Convection (labeled region B) increases the size and intensity of the southern black hole. This brings our model yet closer to the observations.

As is demonstrated in Takamitsu Ito's paper, the convection in the SPCZ does not affect the tropical black holes very much, serving mostly to trim off the southwest corner of the southern black hole. Convection in the South Pacific is generally less stable and more prone to advection. We found (and will describe later) that the response of the subsidence field to forcing becomes slower, smaller, and concentrated to the west as one moves poleward from the equator, so that the fluctuating SPCZ does not have much of an effect on the East Pacific subsidence fields.

As we observe a rather gentle evolution of the ITCZ convection in Figures 1 - 3, forcing function F4 is the most appropriate. γ was selected so that the period of forcing is 5 days. We are particularly interested in days 2-4, in which the convection reaches a maximum and then begins to decay. S_0 was set so that the average intensity of the forcing is consistent with the experiment measurements.

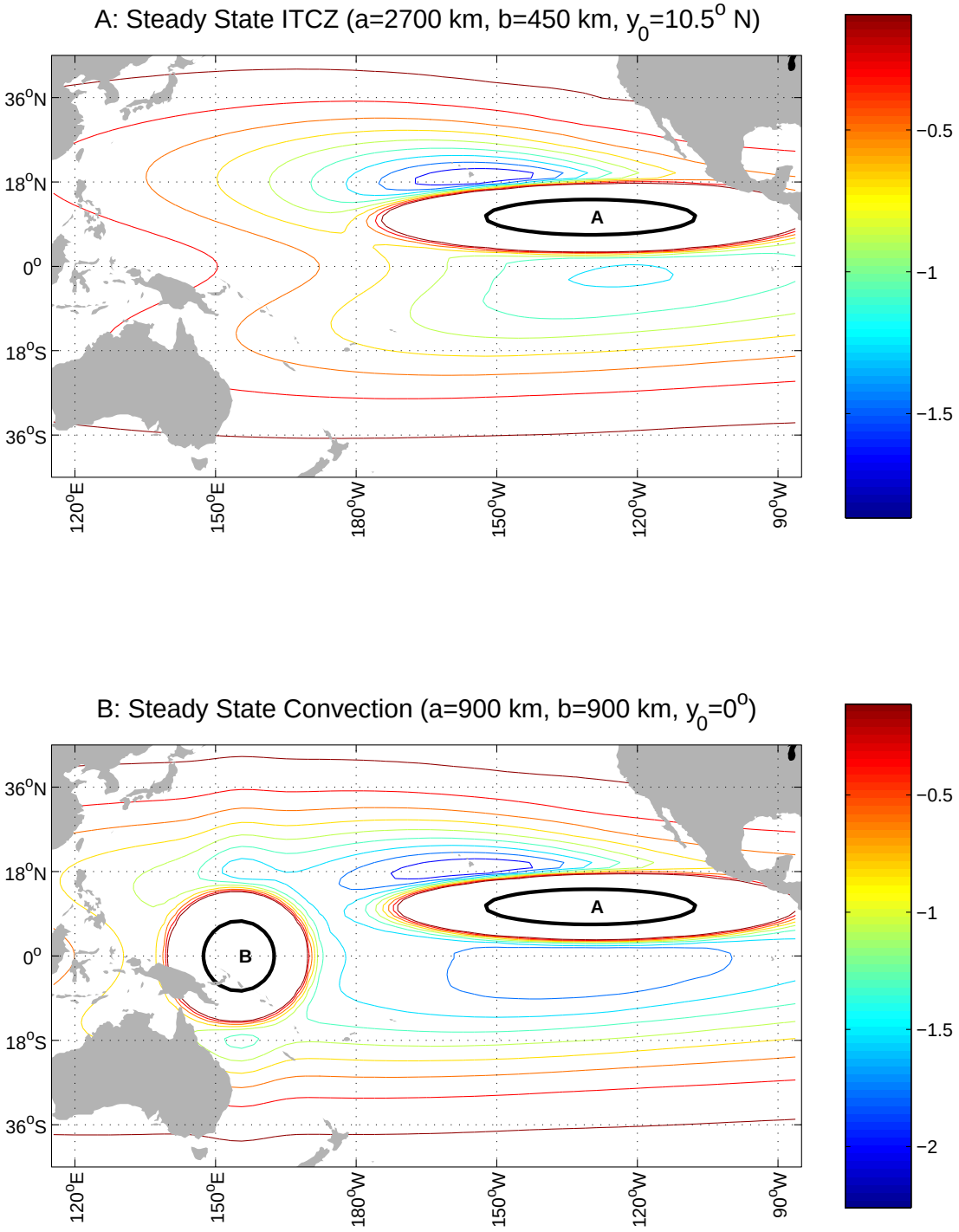

Figure 5: Subsidence (m/day) in Steady State Solutions

3.3 The Time Dependent Simulation

Figures 6 through 11 show the subsidence fields in increments of one day. The small cartoon in the bottom left hand corner of each figure illustrates the path of the forcing function, the marker showing the current intensity. Subsidence in each figure is given in m/day. It should be noted that our analytic technique gives us an exact solution for any time we choose, so that each field is equally accurate. For the discussion in this section, we will equate low humidity in the upper troposphere with subsidence.

We begin in Figure 6 with the steady state response of the West Pacific convection. When the East Pacific convection begins, there is initially very little east-west or north-south asymmetry in the subsidence field. (This will be further illustrated in the next section.) After one day, Figure 7, some asymmetry has developed, but the solution is more balanced than in the steady state. Note that the initial response is predominantly north and south of the ITCZ.

By day 2, Figure 8, the response has spread further east and west, and the characteristics of the steady state solution have developed. As we saw in Figures 1 and 2, the subsidence region to south of the ITCZ is much larger, and centered east of the small northern black hole.

When the convection begins to decline, as in Figure 9, we see the fastest response in the south east. The peak subsidence in the southern black hole has pushed from 120^0 to 145^0 W. A second peak region of subsidence has moved east over South America, and will propagate further east over the next few days of the simulation. This is a Kelvin wave packet! It may be difficult to observe this movement in the real atmosphere, as there is significant convection over the Amazon Basin.

By day 4, Figure 10, subsidence has ceased over much of the East Pacific, but held strong in the west. It is remarkably consistent with Figure 3, in which the eastern half of the southern black hole decays when the convection ceases. The northwestern subsidence regions slowly propagates further westward, as seen in Figure 11, again consistent with the movement of the actual northwestern black hole. Here we have a Rossby wave packet. We also note that the subsidence lingers in the north much longer than in the south; the asymmetry of the steady state has reversed.

3.4 Subsidence and Humidity?

In the steady state, the link between subsidence and humidity in the upper troposphere has been established empirically. In our time dependent simulation, we tread upon shakier ground in making comparisons. Our model only tells us the subsidence rate. In the future we must study the time dependence between subsidence and the drying of the upper troposphere. How long does it take the upper troposphere to dry out after subsidence begins, or moisten after it ceases? We may need to look at the full vertical motion field to obtain sound results.

3.5 Component Analysis

The Matsuno formulation of the equatorial β-plane response allows one to separate the atmospheric response into components, specifically the effect of Kelvin, Rossby, and westward

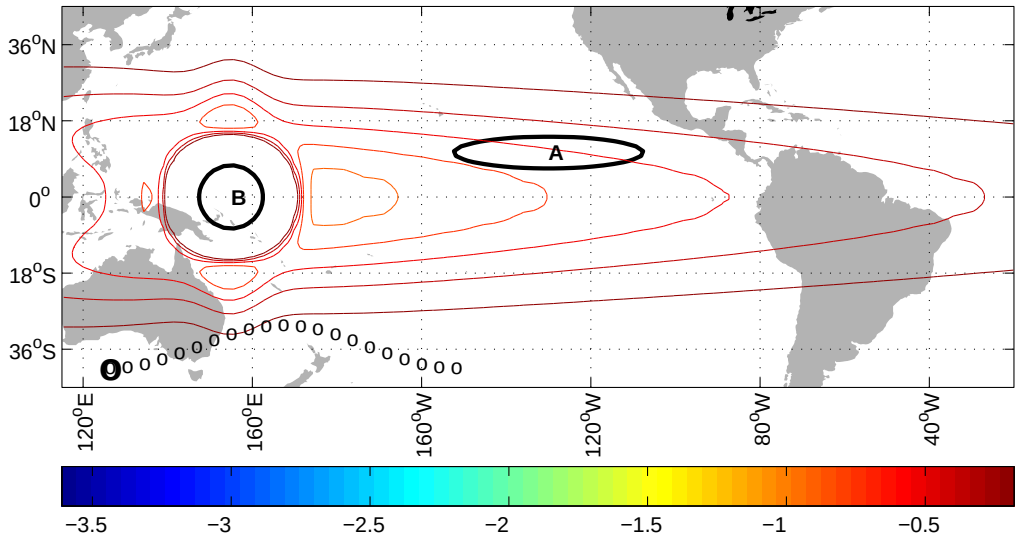

Figure 6: Full Solution, Time = 0

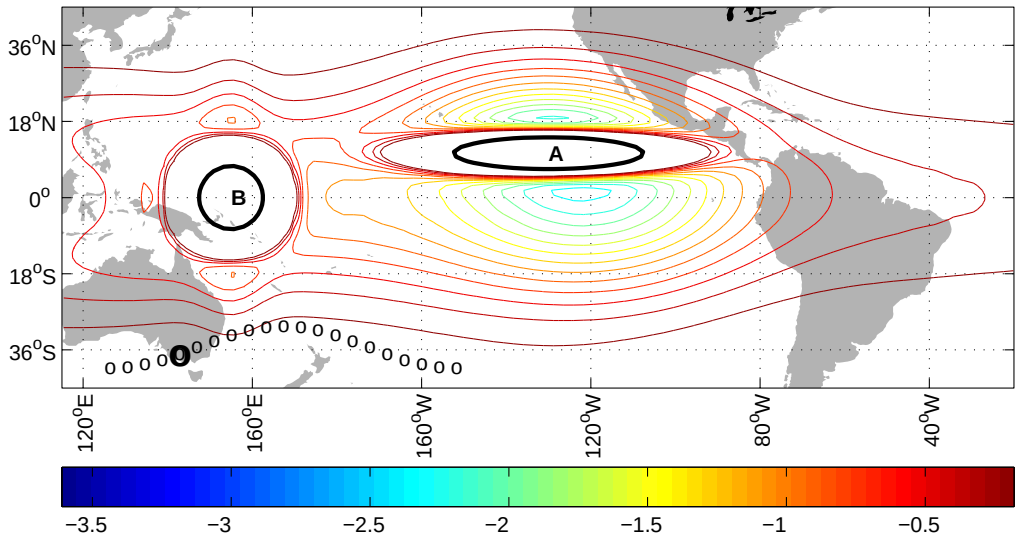

Figure 7: Full Solution, Time = 1 day

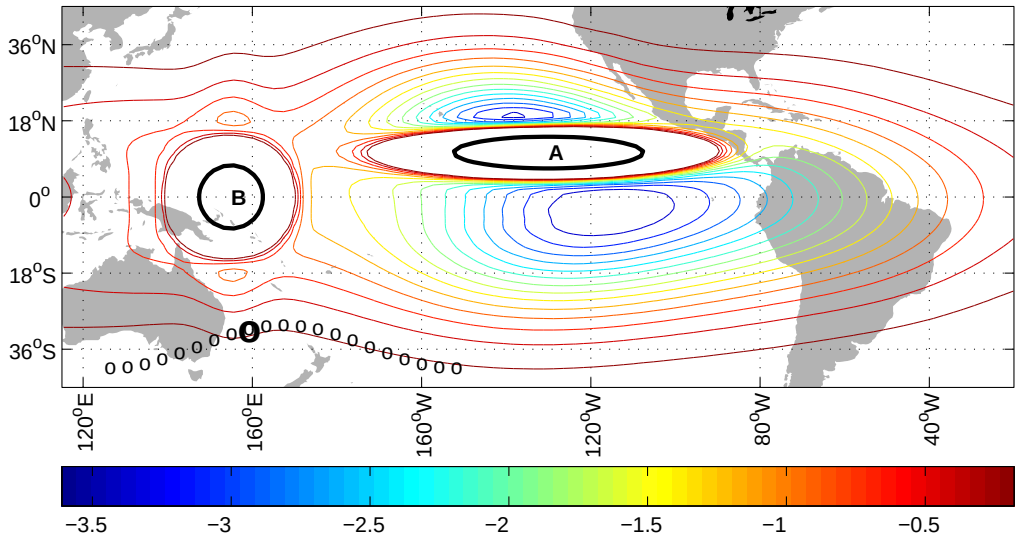

Figure 8: Full Solution, Time = 2 days

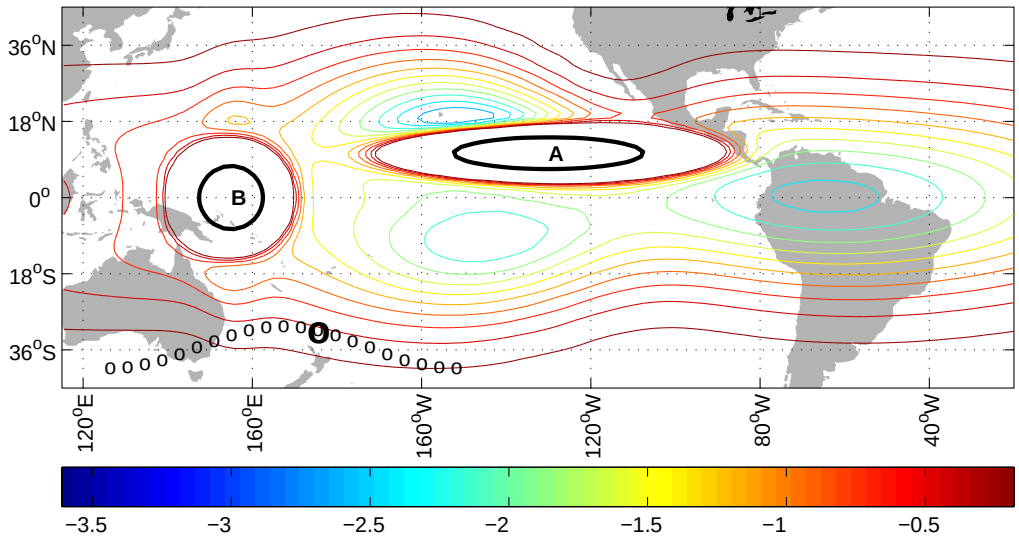

Figure 9: Full Solution, Time = 3 days

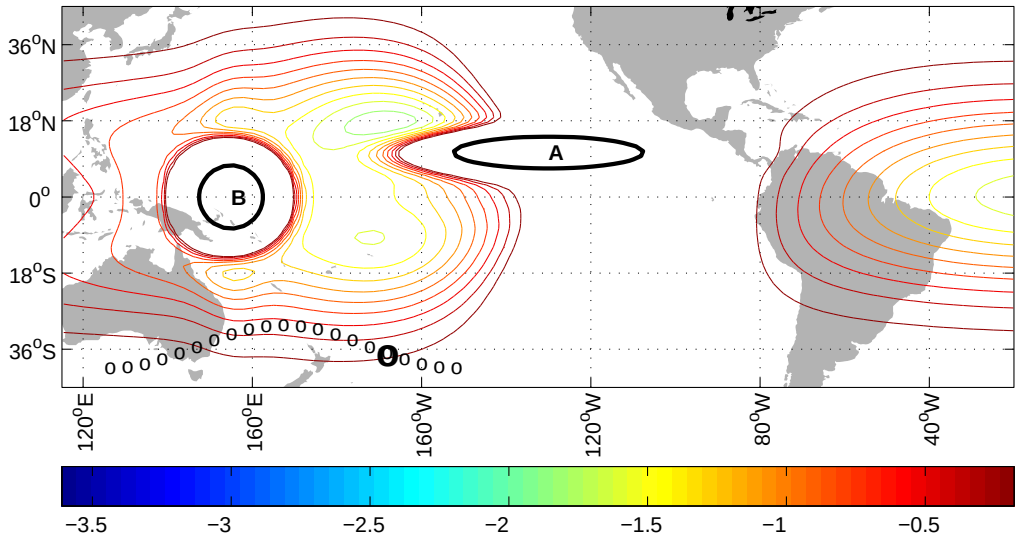

Figure 10: Full Solution, Time = 4 days

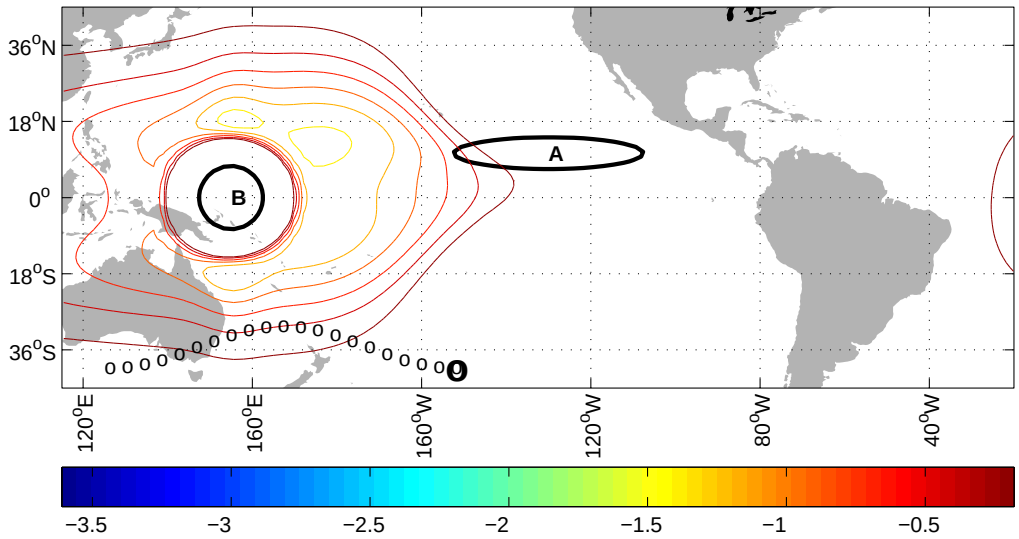

Figure 11: Full Solution, Time = 5 days

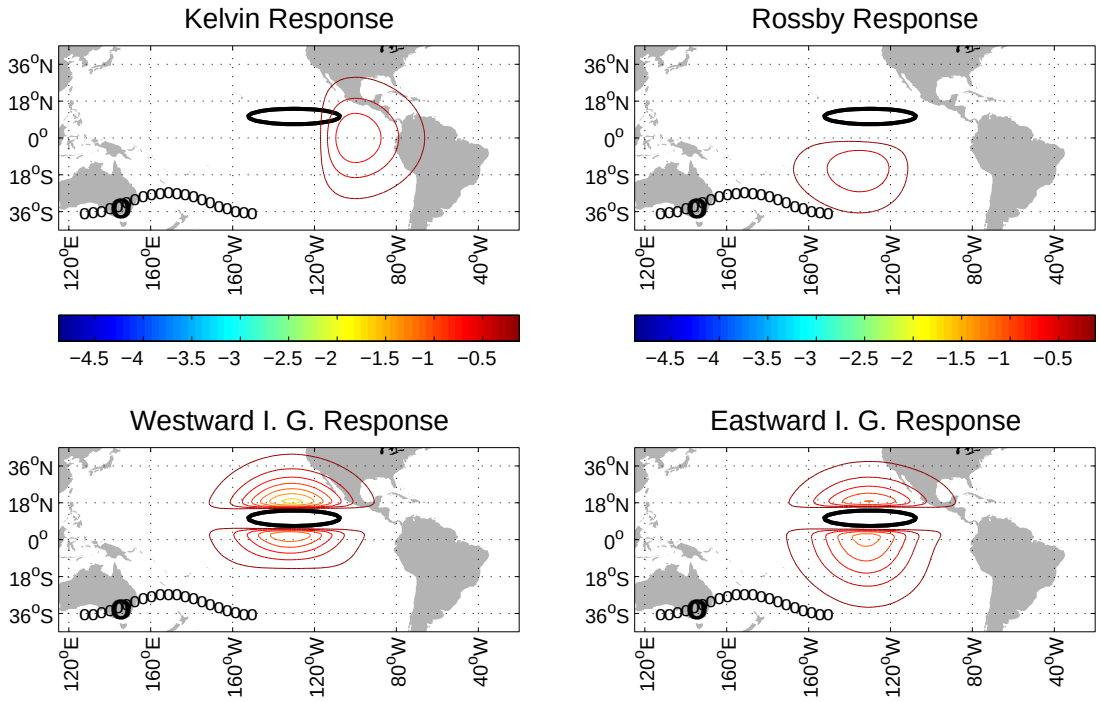

Figure 12: Components, Time = 1 day

and eastward propagating inertial gravity waves. In Figures 12 to 15 we present the total response to each type of wave. Note that the total subsidence fields is not necessarily the sum of these fields, as we have not shown the regions in which air is rising.

The east-west asymmetries in the response are the result of differences between Kelvin and Rossby waves. The Kelvin response grows much faster than the Rossby response, as one would expect based on the group velocities at which they propagate. The group velocity of nearly nondispersive long Rossby waves of order n is dwarfed by the Kelvin group velocity by a factor of $1/(2n+1)$ for $n > 0$. As the forcing decays, we see the Kelvin response propagating off to the east in a coherent packet.

The Rossby response focused south of the forcing is due to contribution from the $n = 0, r = 0$ mixed mode wave, and hence behaves in part like an inertial gravity wave. It dies faster than the other Rossby waves in the end when the forcing decays. The two pronged Rossby response west of the forcing, seen best in Figure 15, is due to the low frequency Rossby waves of order $n = 1$ and above. It becomes the dominant feature at the end of the simulations, explaining the enhanced stability of the western half of a black holes. The northern half of the Rossby packet is the slowest to grow and decay. Higher order Rossby waves, with their low group velocities, generate the response away from the equator.

The relative intensity at which the different wave types are excited is highly dependent on the spatial extent and latitude of the forcing. For instance, Kelvin waves are excited to a larger extent when the forcing is near the equator. Lower order waves are favored in general when the response is broad and near the equator.

As the forcing is moved further poleward, the black hole associated with it will decline

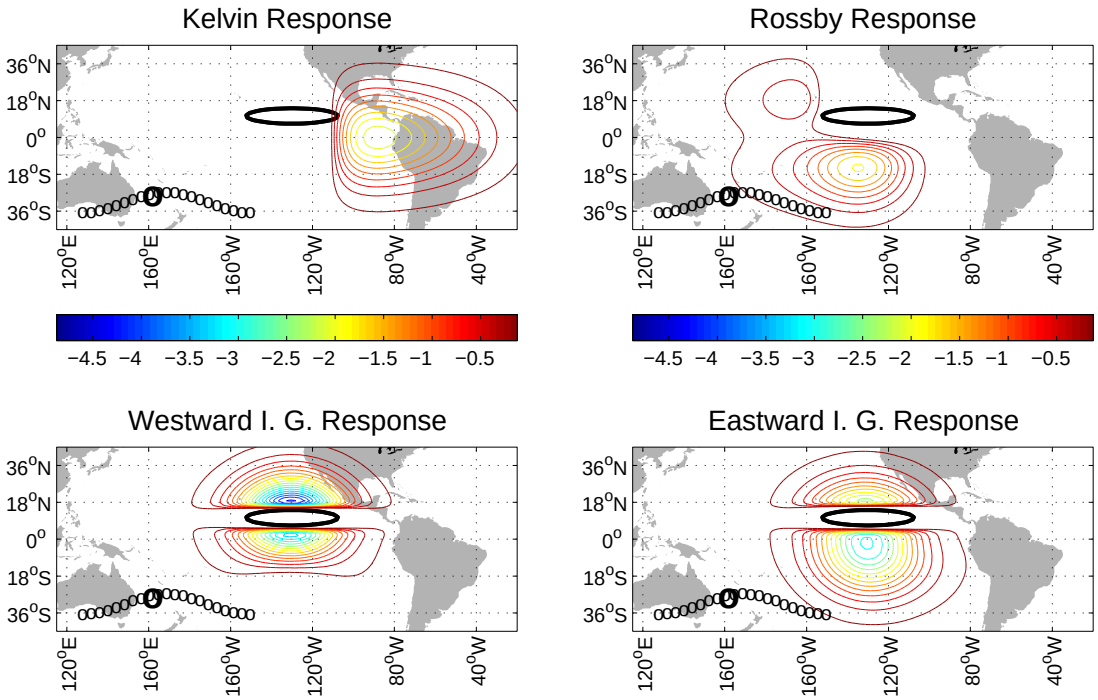

Figure 13: Components, Time = 2 days

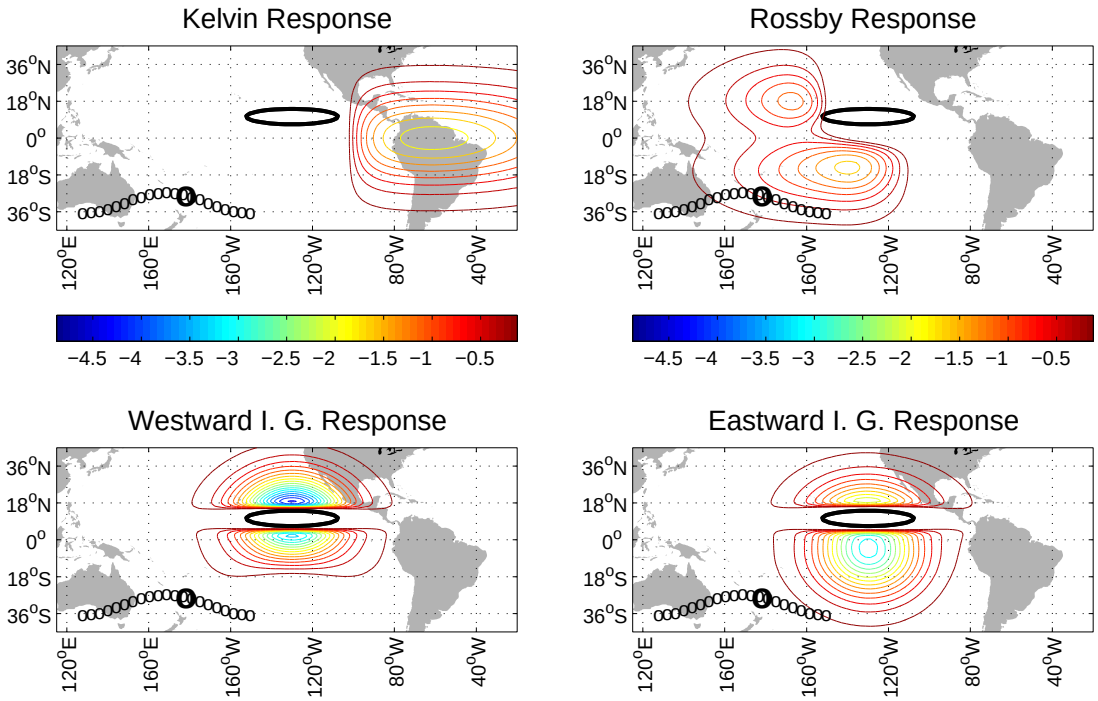

Figure 14: Components, Time = 3 day

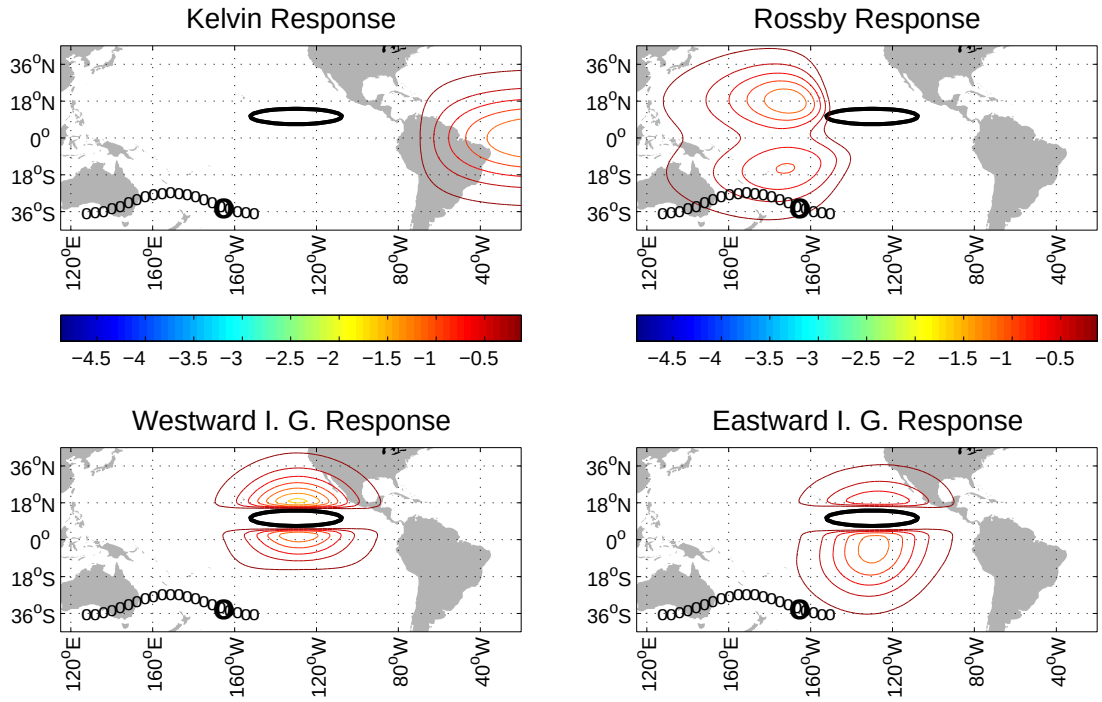

Figure 15: Components, Time = 4 days

in size, gain in local intensity, and move west of the forcing. The shift to the west comes from the fact that Kelvin waves can only be excited near the equator. The decline in spatial extent, which is coupled with an increase in intensity necessary to maintain continuity, can be attributed to the shrinking Rossby radius of deformation. Away from the equator the deformation radius is inversely proportional to the local Coriolis parameter, βy, on our β-plane. At high latitudes the Rossby waves tend to dominate over inertial gravity waves, too. The gravity wave response decreases with the Rossby number, which is also inversely proportional to the Coriolis parameter. Once the forcing is 1 or 2 Rossby radii poleward of the equator, the quasi-geostrophic equations become a good approximation to our system provided that our forcing is broad, and we can neglect inertial gravity waves all together.

3.6 The Time Dependence of the Hadley and Walker Circulations

Flow in the first baroclinic mode takes place in two layers. Air is sucked in from all directions toward the convection region in the lower half of the troposphere, and propelled upward by the convection. It then flows back in the upper half of the atmosphere, subsiding gently into the lower flow over broad regions to complete the cell. The Walker Circulation describes the east-west part of this flow (or perhaps I should say, the east-west flow "is" the Walker Circulation), and the Hadley Circulation is the north-south flow. We define the magnitude of the Walker circulation to be the maximum zonal mass transport toward the convection region in the lower layer, or equivalently, away from the convection in the upper layer. Similarly, we measure the Hadley circulation by the maximum meridional transport.

We can further divide the Walker circulation into western and eastern branches. The western branch is the maximum zonal transport to the convection coming from the west, and hence is due primarily to the Rossby response. The eastern branch tracks the flow from the east, and is generated by the Kelvin response. The Hadley circulation divides into northern (summer) and southern (winter) cells. These cells are established, to the most part, by the interaction of inertial gravity waves and the the mixed Rossby-inertial gravity modes.

As subsidence completes the Walker and Hadley circulations, the asymmetries of the meridional and zonal flows are the same as those we see in the formation of black holes. Calculating the flows thus gives a quantitative measure of the black hole asymmetries. For each forcing function we plotted the intensity of the four cells as a function of time relative to their steady state values. The total transports east-west and north-south at steady state are roughly equivalent so that the units in both diagrams are effectively the same.

For example, in the plots of the northern and southern branches of the meridional circulation, 1 unit on the y-axis corresponds to the total mass transport at steady state. The total is the sum of the absolute values of both cells, and hence corresponds to the total mass drawn into the convection region. The sign for transport in the northern cell is negative because mass is moving southward toward the convection region in the lower layer. The zonal mass transports are also plotted relative to the total steady state transport. The eastern branch is negative, as mass is moving to the west.

Forcing function F1 presents the unrealistic adjustment problem. As shown in Figure 16, the meridional transport is initially quite unstable. The inertial gravity waves slosh the circulation back and forth as they adjust to the sudden shock. While the meridional circulation reaches values comparable to the steady solution almost instantaneously, the zonal transport lags behind, and has not reached the steady state values after 2.5 days of simulation.

In the lower half of Figure 16, we compare the dissipation limited growth to the growth of the zonal mass transport. If the frequency ω is small relative to ϵ, our forcing function reduces to

$$\tilde{S}(t) = S_0 \frac{1 - e^{-(\epsilon + i\omega)t}}{\epsilon + i\omega} \rightarrow \frac{1 - e^{-\epsilon t}}{\epsilon}, \tag{88}$$

and growth is controlled by the friction. This will only hold for the full solution if it holds for all modes. Clearly it is not the case, for the friction dominated curve should match that of the total transport.

The response to forcing function F2, as pictured in Figure 17, is also quite unrealistic. The meridional response is not quite as instantaneous, but still sloshes back and forth. We compare both the meridional and zonal decay rates to the dissipation dominated spin down,

$$\tilde{S}(t) = S_0 e^{-(\epsilon + i\omega)t} \frac{1}{\epsilon + i\omega} \rightarrow \frac{e^{-\epsilon t}}{\epsilon}. \tag{89}$$

While the curve does not match for the Hadley circulations, it gives a pretty sound fit for the decay of the Walker cells. This indicates that the the bulk of the Rossby and Kelvin response at steady state is controlled by low frequency waves. As indicated by the poor fit in Figure 16, higher frequency modes were important at the onset of forcing.

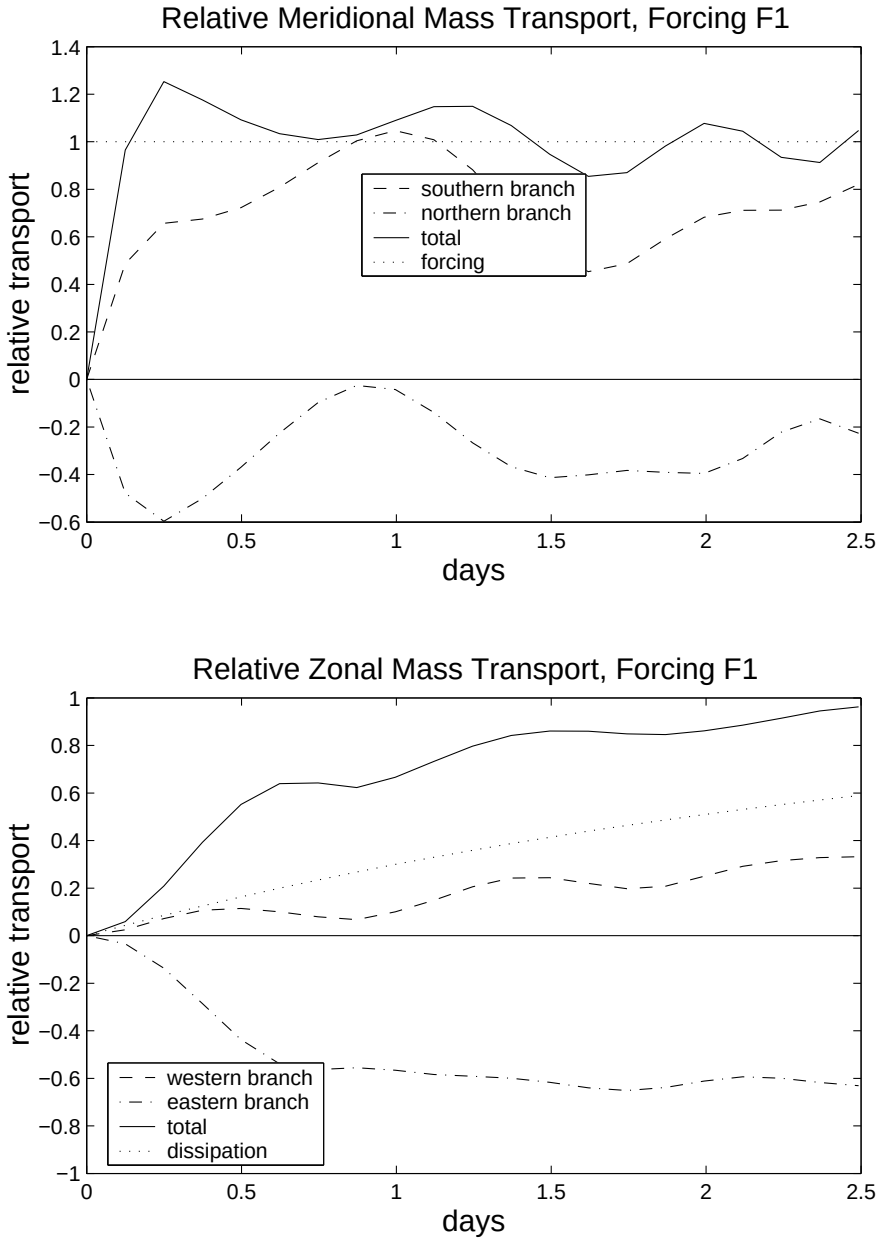

Figure 16: Hadley and Walker Circulations, Forcing Function F1

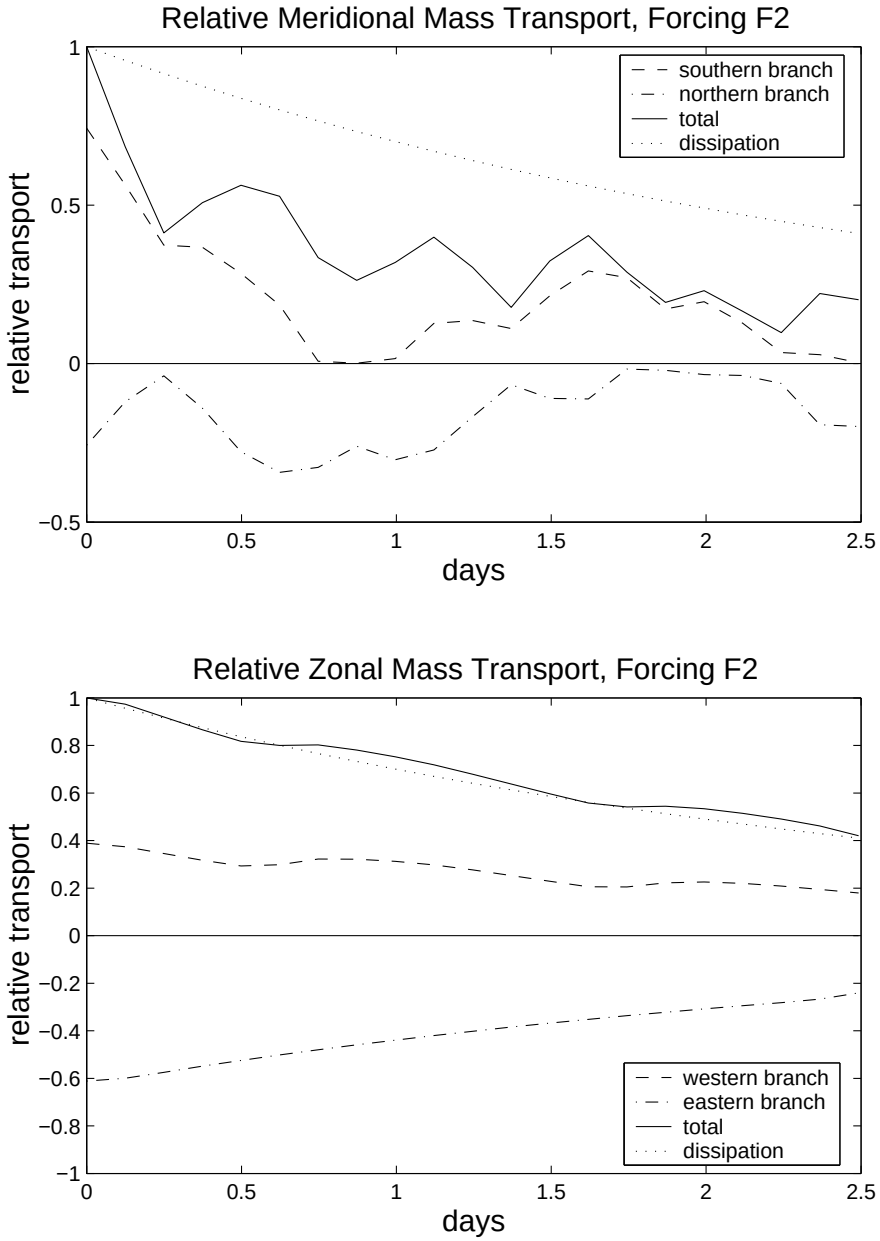

Figure 17: Hadley and Walker Circulations, Forcing Function F2

Forcing function F3 presents a more realistic rise to steady state convection. In the upper half of Figure 18 we find the meridional circulation nearly perfectly in step with the forcing. There are still some oscillations due to the abrupt start. These oscillations are absent with the smooth forcing F4, as shown in Figure 20. As shown in the bottom half of 18, the Walker circulation lags behind the forcing by 1-2 days.

A close look at Figure 19 reveals that northern and southern cells of the Hadley circulation are nearly symmetric at the onset of convection. Figure 19 better illustrates this phenomenon. We present the ratio between the two branches of the Hadley and Walker circulations as a function of time. The horizontal lines indicate the steady state ratios. For instance, at steady state, the southern branch of the Hadley circulation is nearly 3 times stronger than the northern half. In the beginning, however, the north and south cells are nearly equal. The $n = 0$ mixed mode response accounts for much of the steady state asymmetry, and takes longer to establish itself.

The west-east asymmetry also evolves with time. It begins close to its steady state value, and then drops to a point where the eastern cell is five times larger than its western counterpart. This can be attributed to the larger group velocity of Kelvin waves, which gives the eastern branch a quicker start. The initial surge by the Rossby wave is due to the mixed mode. It is slower than the other gravity waves, but faster than Rossby and Kelvin waves!

Lastly we look at response to the smooth forcing F4, shown in Figures 20 and 21. While the total meridional circulation is nearly in perfect step with the forcing, the zonal circulations lag, the Eastern cell by 1/2 a day, the western cell by over a day. In this trial in took 1.5 days to establish the north-south asymmetry - the acceleration of the forcing function seems to promote a symmetric response. Note that the drop in the north-south ratio at the left of Figure 21 is due to a problem in how we calculated the ratio, and is not at all physical. The west-east ratio curve appears similar to that in Figure 19.

4 Limits of our Theory

4.1 The Nonlinear Terms

We have neglected the advective terms in the shallow water equations throughout our analysis. We must ask what differences we should expect in a solution of the complete equations,

$$\frac{\partial u}{\partial t} - yv + \frac{\partial h}{\partial x} = -\epsilon u - (u\frac{\partial u}{\partial x} + v\frac{\partial u}{\partial y}) \tag{90}$$

$$\frac{\partial v}{\partial t} + yu + \frac{\partial h}{\partial y} = -\epsilon v - (u\frac{\partial v}{\partial x} + v\frac{\partial v}{\partial y}) \tag{91}$$

$$\frac{\partial h}{\partial t} + \frac{\partial u}{\partial x} + \frac{\partial v}{\partial y} = -\epsilon h - S - (u\frac{\partial h}{\partial x} + v\frac{\partial h}{\partial y}). \tag{92}$$

As a first line of inquiry, we calculate the magnitude of the nonlinear terms given our final solution. They must be much relatively small for our solutions to be at least self-consistent. Table 4.1 lists the worst case ratio of the magnitude of the nonlinear terms to

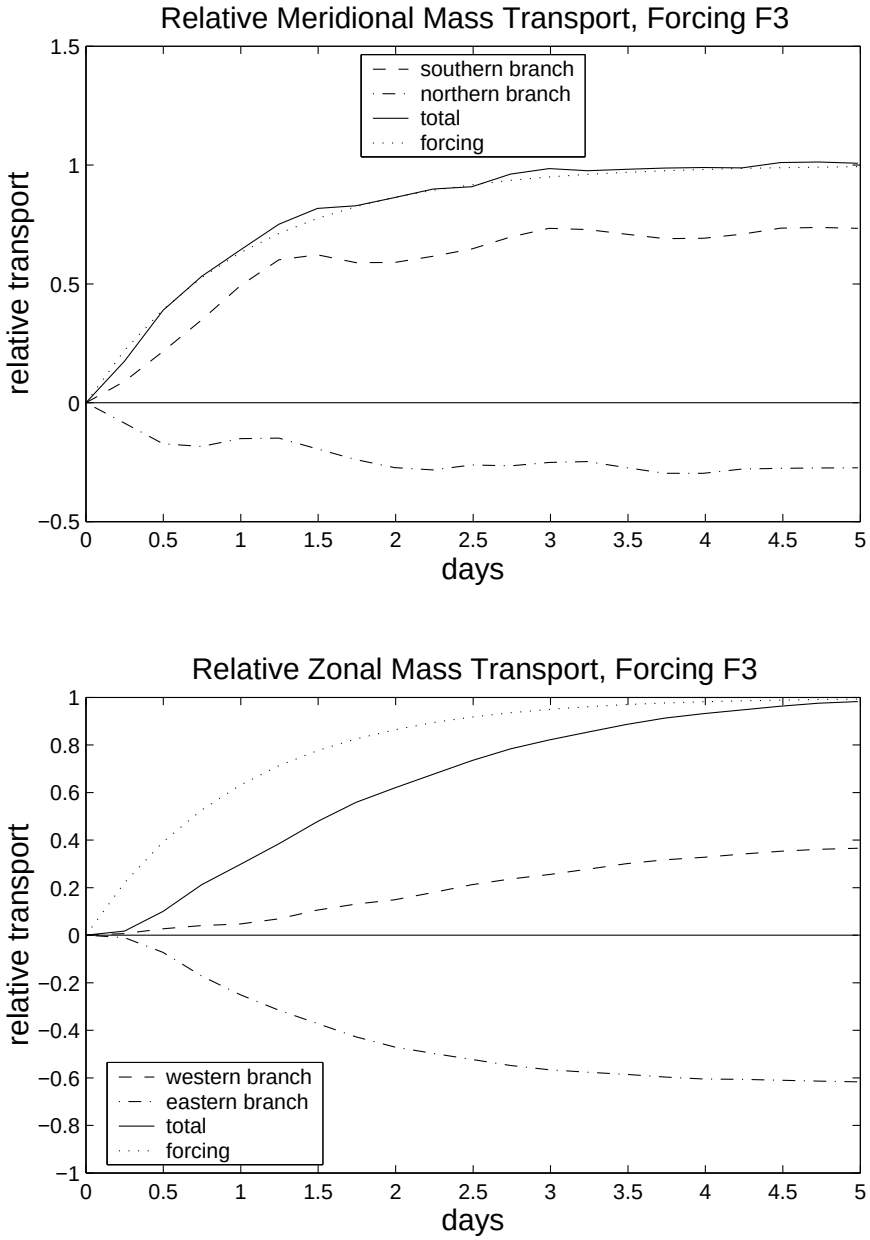

Figure 18: Hadley and Walker Circulations, Forcing Function F3

	Ratio $\frac{nonlinear}{linear}$
x-momentum	30%
y-momentum	7%
mass conservation	4%

Table 2: Relative Size of the Nonlinear Terms

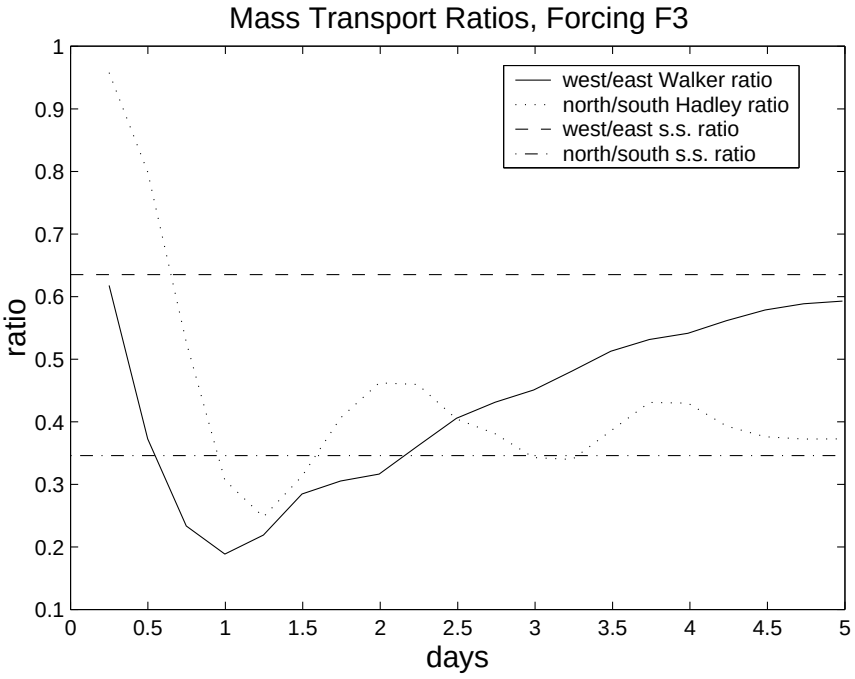

Figure 19: Asymmetries in the Circulation, Forcing Function F3

the combined magnitude of the linear terms for each of (90) - (92), as calculated by finite differencing the linear, steady state solutions.

With the exception of (90), the nonlinear terms are small enough to justify neglecting them. In (90), the nonlinear terms are the most problematic on the equator where subsidence is strongest in the southern black hole, as illustrated in Figure 22. The loss of the Coriolis force on the equator makes this region particularly susceptible to nonlinearities. In addition, the upward velocity, given by (65), is large in regions where partial derivatives u_x and v_y are strong. As such partials are present in the nonlinear terms, we should expect them to be strong in regions of subsidence.

4.2 Susceptibility to Barotropic Instability

As friction plays a small role in our system of equations, we can anaylze them in the inviscid limit. We then expect the flow to become susceptible to barotropic instability when there exists a reversal in the potential vorticity gradient. The linear (nondimensional) PV principle in our model was given in (9), with the PV anomaly q defined by (10). q can be calculated in spectral space, as PV is conserved by each unforced mode. (It is important the note that the forcing and dissipation terms serve only to tell us the magnitude of each mode, and do not effect the velocity fields, or the PV!) First, we have that

$$\frac{dq}{dt} + v = 0 \tag{93}$$

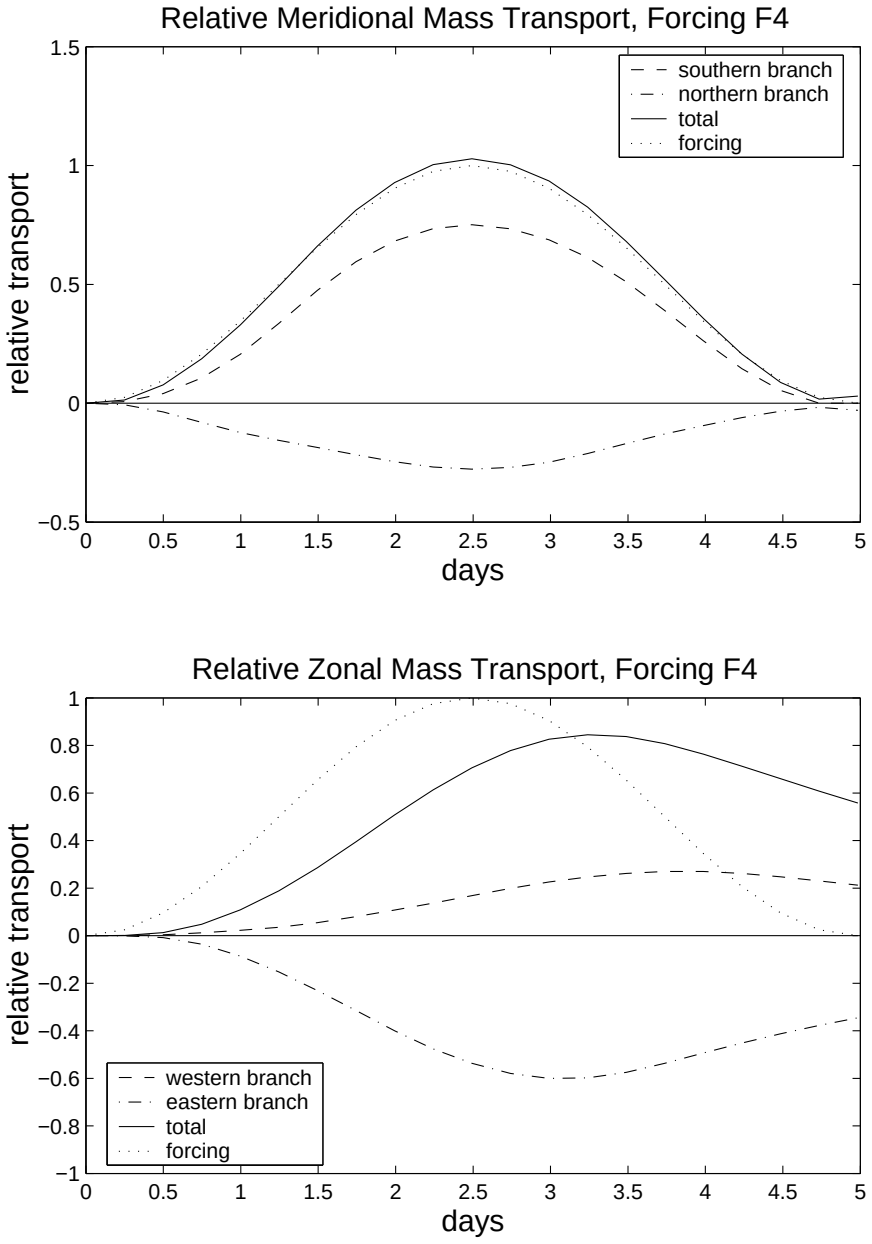

Figure 20: Hadley and Walker Circulations, Forcing Function F4

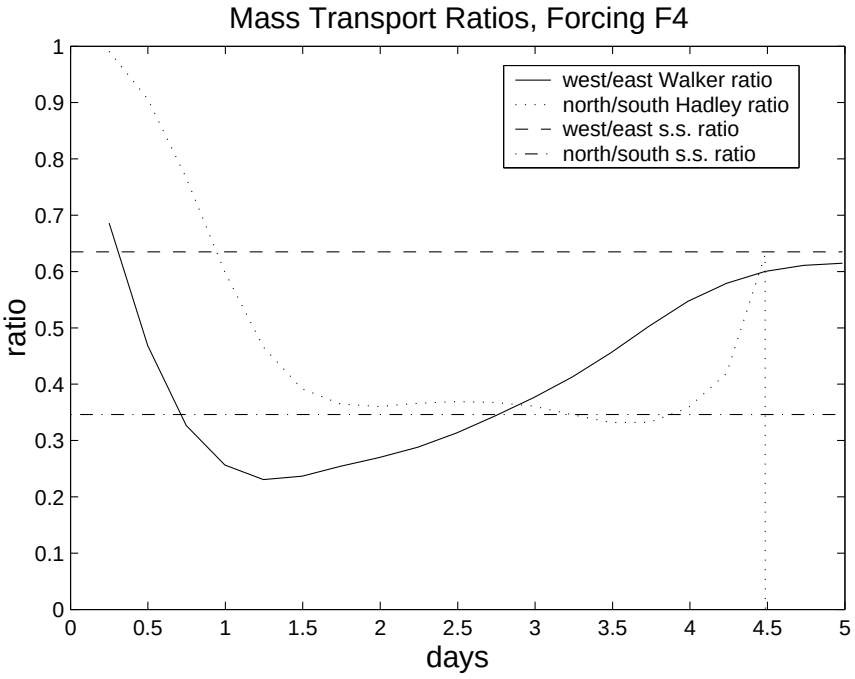

Figure 21: Asymmetries in the Circulation, Forcing Function F4

in the inviscid, unforced problem. Move to Fourier space and write $\hat{q}$ as a sum of the contributions from each normal mode,

$$\hat{q} = \sum_{n,r} \hat{w}_{n,r}(k,t)\mathcal{Q}_{n,r}, \tag{94}$$

to obtain the transform of (93),

$$-i\omega_{n,r}\mathcal{Q}_{n,r} + \mathcal{V}_{n,r} = 0. \tag{95}$$

$\mathcal{Q}_{n,r}$ is the PV contained in the nth, rth normal mode. A quick rearrangement yields

$$\mathcal{Q}_{n,r} = \frac{\mathcal{V}_{n,r}}{i\omega_{n,r}}. \tag{96}$$

Likewise,

$$\frac{d\mathcal{Q}_{n,r}}{dy} = \frac{\frac{d\mathcal{V}_{n,r}}{dy}}{i\omega_{n,r}}. \tag{97}$$

We can then calculate q and $\partial q/\partial y$ as u, v, h, and w before.

The nondimensional PV anomaly q has units $\frac{c}{L} = \left(\frac{\beta}{c}\right)^{\frac{1}{2}}$, while $\partial q/\partial y$ has units of β. Hence, the criterion for a reversal of the total PV gradient in y is that nondimensional $\partial q/\partial y < -1$.

The PV field and gradient in y are shown in Figure 23, which indicates that the first baroclinic mode is linearly stable. The top half of the diagram illustrates the PV field. Note

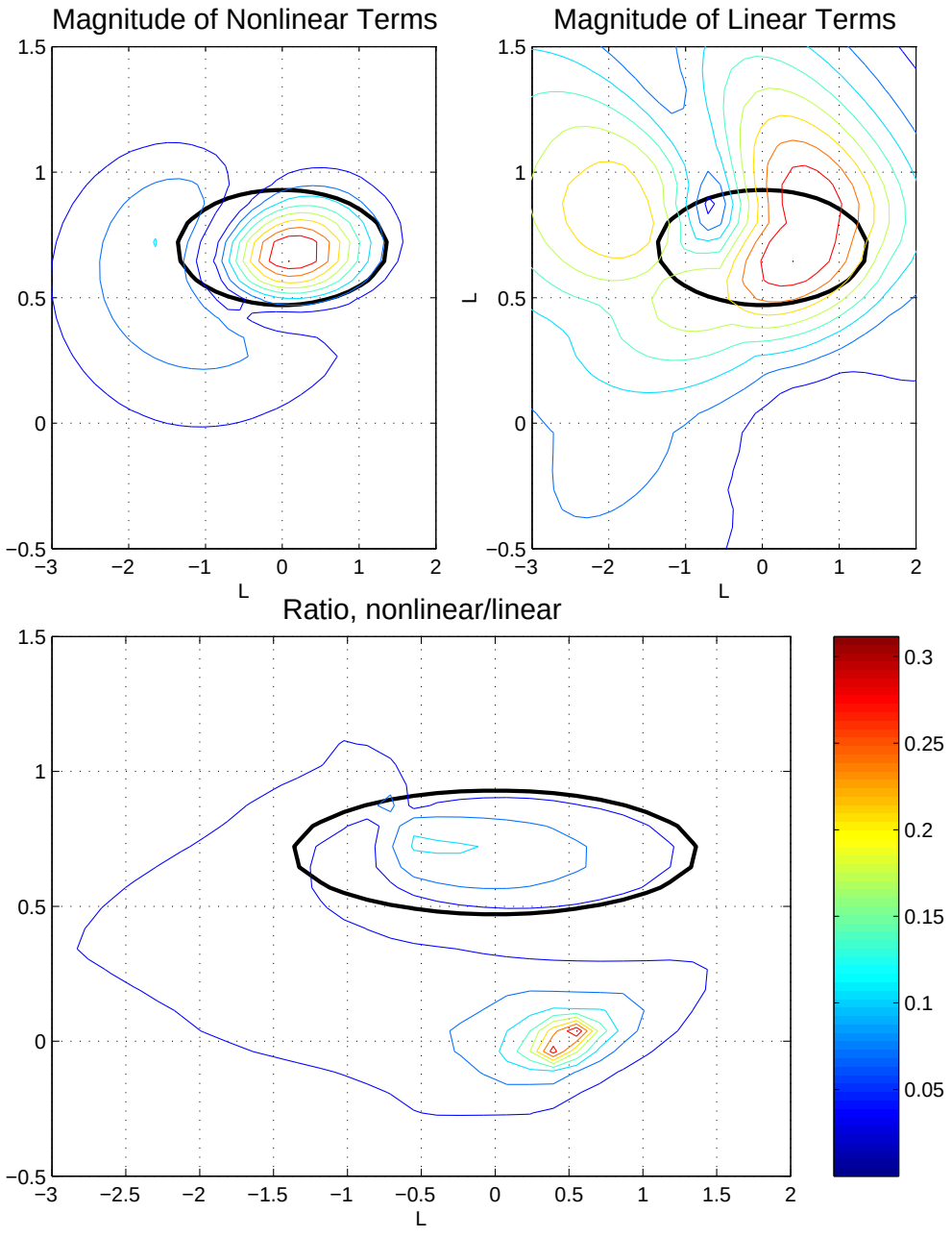

Figure 22: The Nonlinear Terms (Note that we have used nondimensional length units. 1 unit is appoximately 1800 km.)

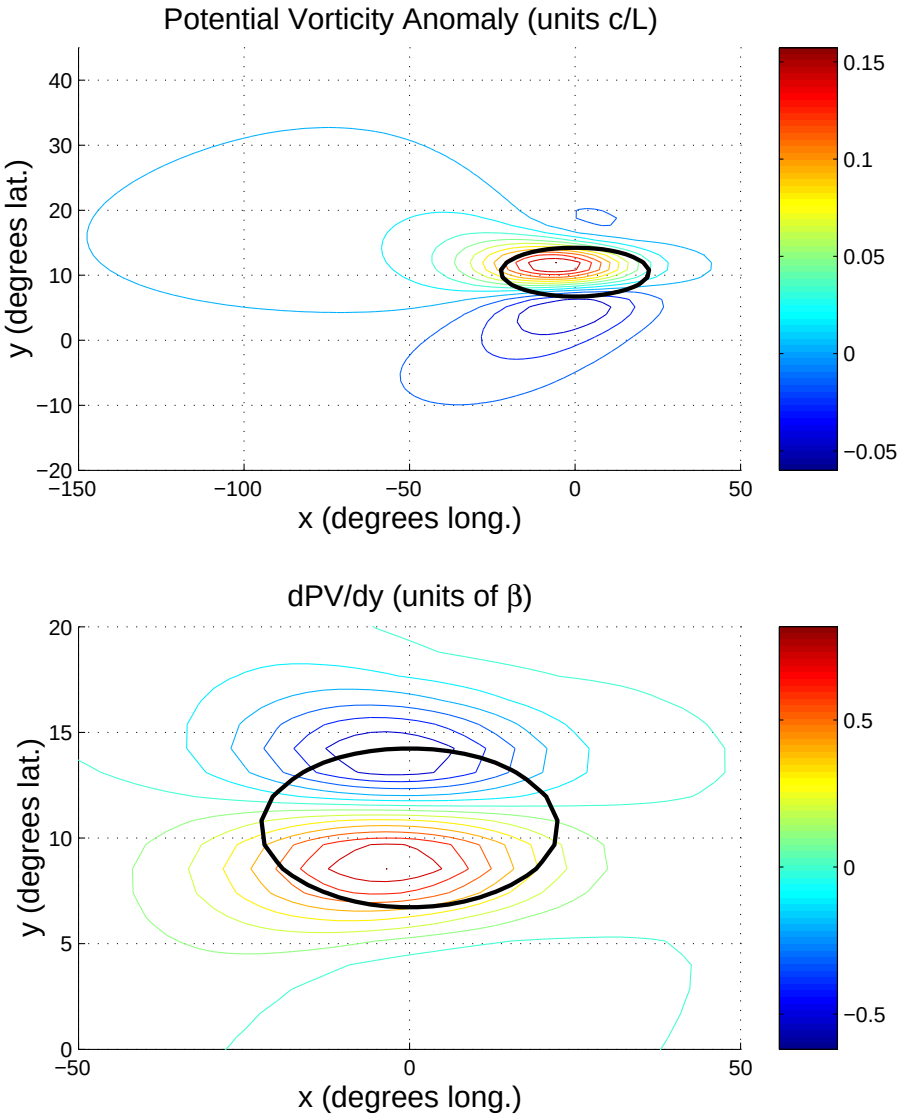

Figure 23: The Potential Vorticity Anomaly

mode	c (m/s)	$\bar{h}$ (m)	S_d (m/day)	S_{nd}
1	77	610	57	0.026
2	47	220	55	0.086
3	31	98	5.6	0.025
4	23	56	3.2	0.053

Table 3: Marshall Island Data

that it is biased heavily to the west and, to a lesser extent, to the north. The east-west asymmetry is more easily explained: Kelvin waves carry no PV, whereas Rossby waves do. The north-south asymmetry can be explained in view of PV stretching. The yS term in our PV principle, (9), corresponds to the stretching of the planetary potential vorticity. The effect becomes more pronounced as the Coriolis force grows with latitude.

4.3 Higher Baroclinic Modes

A study of the atmosphere over the the Marshall Islands gives us a measure of the intensity at which each baroclinic mode is excited by the release of latent heat [1]. The relevant data, shown in Table 4.3, indicates that the bulk of the latent heat release excites the first two baroclinic modes; S_d, the dimensional forcing, indicates the strength of the excitation for each mode.

Recall that the physical scales of the system are determined by c. As c becomes smaller, the length scales shrink and the time scales lengthen. The magnitude of the nonlinear terms and intensity of the PV gradient involve spatial derivatives, and thus are enhanced as the length scales shrink. They are proportional to the nondimensional forcing $S_{nd} = S_d\, g\beta^{-\frac{1}{2}} c^{-\frac{5}{2}}$. Hence for the second baroclinic mode the relative intensity of the nonlinear terms is 3.3 times larger than for the first mode, as is the PV gradient! We should then expect the second baroclinic mode to be nonlinear and potentially unstable, were it to exist by itself. Nonlinearities ruin our ability to paste modes atop each other, making it difficult to say whether the full solution (taking into account the nonlinear terms and all baroclinic modes) would be unstable. Note, however, that w is proportional to S_d, so that the subsidence field is determined by just the first two baroclinic modes.

5 Conclusions

Linear theory has performed remarkably well in revealing the gross features of the time evolution of water vapor black holes. The asymmetries in the growth and decay of the dry regions are readily seen as a ballet of Kelvin, Rossby, and inertial gravity waves.

A better fit to observations could be made by including more baroclinic modes. I am not sure, however, how much more such activity would teach us about the physics of the system. It may, however, prove very instructive to follow further in the footsteps of Gill and linearize about a mean zonal wind, as in [8]. It is difficult to tell if the movement of the real black holes in Figures 1-3 was due to the propagation of wave packets or advection by the easterly Trade Winds. Linearizing about a mean wind may help settle this question.

The response of the Hadley circulation to forcing is much faster than that of the Walker Circulation. In addition, the western branch of the Walker circulation responds slower to forcing that the Eastern branch. While these properties were known before, it is fruitful to extend these insights to the study of black hole formation. Black holes are often associated with the formation and movement of tropical storms [10], which can be viewed as massive centers of convection. The initial subsidence response is driven by inertial gravity waves, and appears north and south of the system, especially in the winter hemisphere. As the storm moves poleward, the effect of gravity waves and Kelvin waves decrease, and we see primarily a Rossby response to the west of the storm.

As a first attempt to apply these insights to a real storm, we tracked the response generated by Typhoon Pabuk over the west Pacific in August, 2001. When the storm formed over the tropics we observe a massive Black hole extending down over northern Australia. As the storm moved north, we then observed the formation of a intense black hole west of the storm, which appeared to be advected around the storm by anticyclonic winds in the upper troposphere. This interaction between tropical storms and black holes presents an exciting area for future study.

6 Acknowledgments

I would like to thank Wayne Schubert and Takamitsu Ito for all their guidance and insight, both in completing this project and in making my summer GFD experience so wonderful. I also would like to thank Joe Keller for invaluable advice and Janet Fields for all her support throughout the summer. Thanks also to Dargan Frierson for assistance in editing this paper. Lastly, I would like to acknowledge the Naval Research Laboratory, Marine Meteorology Division, 7 Grace Hopper Ave, Monterey, CA 93943 for providing the GOES satellite images, Figures 1 - 3.

References

[1] Fulton, S. R. and W. H. Schubert, 1985: Vertical Normal Mode Transforms: Theory and Application. *Mon. Wea. Rev.*, **113**, 647-658

[2] Gill, A. E., 1980: Some simple solutions for heat induced tropical circulation. *Quart. J. Roy. Meteor. Soc.*, **106**, 447-462

[3] Gradshteyn, I. S. and I. M. Ryzhik, 1965: *Table of Integrals, Series, and Products.* Academic Press, New York, p 1067

[4] Hack, J. J., W. H. Schubert, D. E. Stevens, and H. Kuo, 1989: Response of the Hadley Circulation to Convective Forcing in the ITCZ. *J. Atmos. Sci.*, **46**, 2957-2973

[5] Heckley, W. A. and A. E. Gill, 1984: Some simple analytic solutions to the problem of forced equatorial long waves. *Quart. J. Roy. Meteor. Soc.*, **110**, 203-217

[6] Martin, D. W. and B. B. Hinton, 1999: Annual Cycle of Rainfall of the Indo-Pacific Region. *J. Clim.*, **12**, 1240-1256

[7] Matsuno, T., 1966: Quasi-Geostrophic Motions in the Equatorial Area. *J. Met. Soc. Japan*, **44**, 25-43

[8] Phlips, P. J. and A. E. Gill, 1987: An analytic model of the heat-induced tropical circulation in the presence of a mean wind. *Quart. J. Roy. Meteor. Soc.*, **113**, 213-236

[9] Picon, L. and M. Desbois, 1990: Relation between METEOSAT Water Vapor Radiance Fields and Large Scale Tropical Circulation Features. *J. Clim.*, **3**, 865-876

[10] Rosendal, H., 1998: The Black Hole of Water Vapor and its Use as an Indicator of Tropical Cyclone Development and Intensity Changes. http://members.aol.com/Rosendalhe/black.htm, April 17

[11] Schmetz, J. et. al., 1995: Monthly Mean Large-Scale Analyses of Upper Tropospheric Humidity and Wind Field Divergence Derived from Three Geostationary Satellites. *Bull. Am. Met. Soc.*, **76**, 1578-1584

[12] Silva Dias, P. L.,W. H. Schubert, and M. DeMaria, 1983: Large-Scale Response of the Tropical Atmosphere to Transient Convection. *J. Atmos. Sci.*, **40**, 2689-2707